



HAL
open science

Energy analysis and discretization of the time-domain equivalent fluid model for wave propagation in rigid porous media

Ilyes Moufid, Denis Matignon, Rémi Roncen, Estelle Piot

► **To cite this version:**

Ilyes Moufid, Denis Matignon, Rémi Roncen, Estelle Piot. Energy analysis and discretization of the time-domain equivalent fluid model for wave propagation in rigid porous media. *Journal of Computational Physics*, 2022, 451, pp.110888. 10.1016/j.jcp.2021.110888 . hal-03328599v2

HAL Id: hal-03328599

<https://hal.science/hal-03328599v2>

Submitted on 17 Dec 2021

HAL is a multi-disciplinary open access archive for the deposit and dissemination of scientific research documents, whether they are published or not. The documents may come from teaching and research institutions in France or abroad, or from public or private research centers.

L'archive ouverte pluridisciplinaire **HAL**, est destinée au dépôt et à la diffusion de documents scientifiques de niveau recherche, publiés ou non, émanant des établissements d'enseignement et de recherche français ou étrangers, des laboratoires publics ou privés.

Energy analysis and discretization of the time-domain equivalent fluid model for wave propagation in rigid porous media

Ilyes Moufid^{*,a,b}, Denis Matignon^b, Rémi Roncen^a, Estelle Piot^a

^a ONERA/DMPE - Université de Toulouse, 31055 Toulouse, France

^b ISAE-SUPAERO - Université de Toulouse, 31055 Toulouse, France

Abstract

The equivalent fluid model (EFM) describes the acoustic properties of rigid porous media by defining the intra-pore fluid phase as a fluid with an effective density and an effective compressibility. Their definitions are based on the dynamic tortuosity α and the normalized dynamic compressibility β . These physical quantities are complex-valued functions depending on the frequency, and can be irrational as in the Johnson-Champoux-Allard-Pride-Lafarge (JCAPL) model. Hence, the system of equations derived from the EFM can involve fractional derivatives in the time domain. This paper presents an approach to formulate the EFM equations described by the JCAPL model in the time domain, leading to an augmented system for which a proof of stability is given. From the EFM, a model for numerical simulation is built with α and β approximated using a multipole model. Sufficient stability conditions are then provided for the multipole-based EFM. Lastly, a numerical analysis is carried out in order to illustrate the theoretical results and a simulation of the impedance tube experiment is presented.

1 Introduction

Porous media are abundantly present in nature, and studied in various research fields (e.g. mechanics [23], geosciences [17, 62], biophysics [29, 31, 60]). Porous media are also studied and manufactured for their acoustic properties, which have been used extensively in room acoustics [48] and more recently in aeronautics [56, 64, 70].

In the general case of porous media with a fluid phase and a solid phase in motion, the macroscopic acoustic behaviour is described by the Biot theory [9, 10]. In practice, the rigid-frame case described by the simpler equivalent fluid model (EFM) [2] can be used as a good approximation in a wide range of applications [7]. When the rigid-frame hypothesis is assumed, only the fluid phase of porous media is considered in the description of the acoustic behaviour of the material. Adopting a macroscopic view, the material becomes equivalent, in terms of acoustic behaviour, to that of a fluid with a complex-valued effective density and compressibility. Indeed, these physical properties are frequency-dependent functions and are conveniently expressed by means of the dynamic tortuosity α and the normalized dynamic compressibility β . Rewriting the equations controlling the acoustic behaviour of a porous sample with α and β is valuable [73], as it separates the visco-inertial and thermal contributions, respectively.

When additional assumptions are made on the pore shape, the frequency asymptotic behaviour of the foregoing two functions is known in the low (LF) and high (HF) frequency limits [20, 24, 38, 41]. However, except in the simplest cases, no exact definition can be retrieved at all frequencies, and an adequate connection between low and high frequency limits must be adopted. Various semi-phenomenological models predict α and β in the whole frequency range such as the Höroshenkov model [35, 36], the Wilson model [67, 68], or the Johnson-Champoux-Allard-Pride-Lafarge (JCAPL) model [20, 38, 41, 42, 58]. The JCAPL model, which can recover widely used simpler models such as the JCA and JCAL models, relies on 9 physical parameters. This makes it the most complex of the aforementioned models, although the number of parameters can be reduced in the case of porous media with a pore size distribution close to log-normal [35]. However, a theoretical analysis based on the JCAPL model can yield valuable insights on other models, via existing relations linking the models or similarities between them. If the rigid assumption is relaxed, Johnson *et al.* [38] showed that identical complex-valued functions should appear in the Biot model, resulting in the Biot-JKD model where the dynamic tortuosity is described by the JCA model.

*Corresponding author: ilyes.mfd@gmail.com (I. Moufid)

Therefore, the work done to manage the dynamic tortuosity and the dynamic compressibility is similar in both approaches.

Thanks to the Biot theory and the EFM, numerical simulations of wave propagation in porous media can be used to better predict sound attenuation [15] and material intrinsic properties [27, 59]. Although several models exist to describe the acoustic behaviour of rigid porous media in the frequency domain, *time-domain* numerical simulations are more suited to evaluate broadband signals interacting with porous media. In addition, a time-domain representation is necessary in order to take into account non-linear behaviours. The main challenge of working in the time domain arises from irrational terms contained in the complex-valued functions α and β , which behave like fractional derivatives in the time domain. Numerous works [18, 32, 44, 45] have shown that the way to address these irrational functions has been critical for the efficiency of numerical schemes, both in terms of speed and data storage.

To tackle the time-domain representation of irrational transfer functions, a common practice is to use a diffusive representation of their associated convolution operators [46, 53], or an oscillatory-diffusive (OD) representation which covers a wider range of irrational functions [52]. A diffusive representation of convolution operators leads to express them in the time domain by a continuum of diffusive variables. These variables, known as memory variables in geophysics [19] and auxiliary variables in acoustic [25, 69], satisfy a first-order ordinary differential equation (ODE) easier to manage for stability analysis and numerical schemes than an explicit formula of the convolution products. Based on this approach, Blanc *et al.* [13, 14] used a diffusive representation of the shifted fractional derivative involved in the dynamic tortuosity of the JCA model. They proved the well-posedness of the Biot-JKD model and built an approximated model for it, coined Biot-DA (diffusive approximation) model. Another work done by Ou [54] with a slightly different method based on a Stieljes function representation demonstrates that the JCA dynamic tortuosity admits an integral representation formula (IRF), which can be recast into a diffusive representation.

The discretization of a diffusive representation or of the IRF leads to a multipole model (MM) defined by a discrete sum of elementary first or second-order low-pass systems, also known as IIR filter in digital signal processing [1]. It is parametrized by a set of real or complex conjugate weights and poles, which are computed by a straightforward discretization of the integral using quadrature formulas [11]. Recent works [4, 71] have also directly adopted an MM for the dynamic variables α and β , obtaining the weights and poles by a Padé approximation [66] or a vector fitting algorithm [30] based on experimental measurements. The key idea of working with an MM representation is to obtain a time-domain representation involving convolution products, which can be readily computed using additional first-order ODEs. This technique, originating partly from [16, 21, 39, 57, 63] and classically used for diffusive representation [33] or recently for acoustic metamaterials [8] and dispersive materials [5], has been recently called the auxiliary differential equation (ADE) method [25]. It results in an augmented system which does not require storage of previous time-step solutions and can be solved by classical time-integration schemes. Moreover, the ADE method applied after a minor recasting of the MM expression can ease the numerical computation for schemes based on fluxes, as shown by Xie *et al.* [69].

By taking different approaches, several studies have expressed α and β as an MM but with some distinctions. Zhao *et al.* [71] and Alomar *et al.* [4] worked with the EFM where the effective density and the effective compressibility were approximated as MMs with a set of real and complex conjugate parameters. The real parameters are known to describe dissipative processes, while the complex conjugate parameters were recently shown to be related to locally-resonant behaviour [3]. By contrast, Xie *et al.* [69] used only real parameters to approach the dynamic tortuosity in the Biot-JKD model, a choice justified by the IRF of α . Ou [54] showed that a Padé approximation of the IRF of α can be described by real weights and poles, with a warranty of their signs. Moreover, Blanc *et al.* [13] built the Biot-DA model with the dynamic tortuosity straightforwardly expressed as a real-parameter MM. Then, they proved that their approximated model is stable under the condition of positive real weights. These latter theoretical results with α described by the JCAL model tend to show that both α and β could be well approximated by a real-parameter MM while having a stable and numerically tractable approximated model. Additionally, the JCAL model was proved to be less accurate than the more general JCAPL model for rigid-frame porous medium with cylindrical pores [40], a framework where the exact formula of α and β is given by Zwikker and Kosten [73]. Green's functions calculated based on the effective frequency-dependent wavenumber were used by Kergomard *et al.* to compare the two models in the time domain, leading to a closer approximation of the exact Green's function by the JCAPL model. It thus appears that a time-domain representation with the JCAPL model is desirable. Moreover, to the best of the authors' knowledge, no stability analysis has been conducted on the EFM with the JCAPL model.

In the present work, the rigid-frame hypothesis is taken into account. In Section 2, a brief description of the JCAPL-EFM and the procedure to recast α and β in an oscillatory-diffusive representation [52] are given. An

investigation of the JCAPL-EFM based on the oscillatory-diffusive representation is carried out in Section 3. It brings out the main novelty of the present work by extending the well-posedness proof of the Biot-JKD model [12] for the JCAPL-EFM. Then in Section 4, a multipole-based approximation of α and β is taken and the ADE method is applied following [4, 14, 69]. Next, a stability analysis on the system obtained is performed, giving sufficient conditions on the multipole-based approximation to ensure the stability of the approximated EFM. In Section 5, the validity and the efficiency of the proposed approach is demonstrated numerically, with a Discontinuous Galerkin finite element method combined to a Runge-Kutta time scheme. Finally, a conclusion is drawn in Section 6.

2 Wave propagation in rigid porous media

The EFM is first recalled. Then, the details of the JCAPL model chosen to describe the dynamic tortuosity α and normalized dynamic compressibility β are given. Next, an oscillatory-diffusive representation of the previous functions is taken to get rid of irrational terms and perform a stability analysis. The techniques and procedure used in this section are gathered in Monteghetti's work [49, Chap. 2.1], which were applied to a wide range of acoustical models [52]. Moreover, all equations are written in the Laplace domain in this section. Hence, it is recalled that the one-sided Laplace transform of a locally integrable function G with finite exponential growth, i.e. $G \in L^1_{loc}([0, \infty))$ with $|G(t)| < A e^{\sigma_G t}$, is defined as $\widehat{G}(s) := \int_0^\infty G(t) e^{-st} dt$ in the right half-plane $\Re(s) > \sigma_G$, with σ_G the convergence abscissa.

2.1 Johnson-Champoux-Allard-Pride-Lafarge equivalent fluid model

The frequency-dependent equations controlling the equivalent acoustic behaviour of a rigid porous material are expressed in the Laplace domain:

$$\begin{cases} \rho_0 \alpha(s) s \widehat{\mathbf{u}} &= -\nabla \widehat{p}, \\ \chi_0 \beta(s) s \widehat{p} &= -\nabla \cdot \widehat{\mathbf{u}}, \end{cases} \quad (1)$$

where ρ_0 is the fluid density and χ_0 is the adiabatic compressibility. The macroscopic fluid velocity $\mathbf{u}(t, \mathbf{x})$ and the acoustic pressure $p(t, \mathbf{x})$ obtained by averaging the microscopic velocity and pressure fields over a representative elementary volume, are defined on $(0, \infty) \times \Omega$ with $\Omega \in \mathbb{R}^n$. Note that the porous medium is considered isotropic at the macroscopic scale herein, so α is a scalar term. Moreover, only the interconnected pore network is considered in this work. Dead-end pores and isolated pores, often present in consolidated media, are not considered. The JCAPL model gives an expression of the equivalent density $\rho_0 \alpha$ and the equivalent compressibility $\chi_0 \beta$ based on the dynamic tortuosity (2) and the normalized dynamic compressibility (3), respectively. The physical quantities α and β are intrinsically defined in the frequency domain ($s = i\omega$) and expressed in the time domain by convolution operators.

$$\alpha(s) := \alpha_\infty \left[1 + \frac{\nu \phi}{k_0 \alpha_\infty} \frac{1}{s} \left(1 - \frac{2k_0 \alpha_\infty}{\phi \Lambda^2 \left(\frac{\alpha_0}{\alpha_\infty} - 1 \right)} + \frac{2k_0 \alpha_\infty}{\phi \Lambda^2 \left(\frac{\alpha_0}{\alpha_\infty} - 1 \right)} \sqrt{1 + \frac{\Lambda^2}{\nu} \left(\frac{\alpha_0}{\alpha_\infty} - 1 \right)^2 s} \right) \right], \quad (2)$$

$$\beta(s) := \gamma - (\gamma - 1) \left[1 + \frac{\nu \phi}{k'_0 \text{Pr}} \frac{1}{s} \left(1 - \frac{2k'_0}{\phi \Lambda'^2 (\alpha'_0 - 1)} + \frac{2k'_0}{\phi \Lambda'^2 (\alpha'_0 - 1)} \sqrt{1 + \frac{\Lambda'^2}{\nu} \text{Pr} (\alpha'_0 - 1)^2 s} \right) \right]^{-1}, \quad (3)$$

where the physical parameters are: the kinematic viscosity ν , the porosity ϕ , the high-frequency limit of the tortuosity α_∞ , the static viscous permeability k_0 , the characteristic viscous length Λ , the static viscous tortuosity α_0 , the heat capacity ratio γ , the static thermal permeability k'_0 , the characteristic thermal length Λ' , the static thermal tortuosity α'_0 and the Prandtl number Pr. Hereafter, system (1) with α and β given by (2) and (3) is referred to as the JCAPL-EFM.

Not to mention the large number of parameters, the intricacy of (2) and (3) comes mainly from the irrational nature of the formulas, which share common features with fractional derivatives in the time domain. This makes the stability analysis trickier, since the conventional methods do not work on systems with fractional differential operators. An approach to tackle fractional derivatives is to work with their diffusive representation [46, 47]. The next subsection is therefore dedicated to recasting (2) and (3) under a form which proves more tractable for a stability analysis, and also for time-domain numerical schemes.

2.2 Oscillatory-diffusive representation of the dynamic variables

Before looking at α and β , the example of the function $q : s \rightarrow 1/\sqrt{s}$ defined on $\mathbb{C}_0^+ = \{s \in \mathbb{C} \mid \Re(s) > 0\}$ is recast as a diffusive representation, obtained by using the residue theorem on a Bromwich contour. The analytic extension of q on \mathbb{C} is therefore needed. However, the square root is multivalued on \mathbb{C} , i.e. two values are possible for any $s \in \mathbb{C}$. Hence, the cut $\Gamma = \mathbb{R}^-$ of the complex plane is chosen, which leads to work with q univalued on $\mathbb{C} \setminus \Gamma$. Then, the computation of the jump $q(\xi e^{-i\pi}) - q(\xi e^{i\pi})$ across the cut Γ ($\xi \in \mathbb{R}^-$) exhibits the diffusive weight μ_q associated with the diffusive representation

$$q(s) = \int_0^\infty \frac{\mu_q(\xi)}{s + \xi} d\xi, \quad \text{with} \quad \mu_q(\xi) = \frac{1}{2i\pi} [q(\xi e^{-i\pi}) - q(\xi e^{i\pi})] = \frac{1}{\pi\sqrt{\xi}} \quad (\xi > 0). \quad (4)$$

More generally, following the terminology of [49] (Chap. 2.1), a meromorphic function $g : \mathbb{C} \setminus (-\infty, \gamma_0] \rightarrow \mathbb{C}$ continuous at the endpoint $\gamma_0 \in \mathbb{R}^-$ and with poles at points s_k , admits an *oscillatory-diffusive* (OD) representation

$$g(s) = \sum_{k \in \mathbb{Z}} \frac{r_k}{s - s_k} + \int_{\gamma_0}^\infty \frac{\mu(\xi)}{s + \xi} d\xi \quad (\Re(s) > 0), \quad (5)$$

under the conditions

$$(i) \quad g \text{ decays uniformly at infinity: } \sup_{|s|=R} |g(s)| \xrightarrow{R \rightarrow \infty} 0, \quad (6a)$$

$$(ii) \quad \text{the weight } \mu(\xi) := \frac{1}{2i\pi} [g(\xi e^{-i\pi}) - g(\xi e^{i\pi})] \text{ satisfies } \int_0^\infty \frac{|\mu(\xi)|}{1 + \xi} d\xi < \infty, \quad (6b)$$

$$(iii) \quad \text{the series based on poles and residues must meet a growth condition.} \quad (6c)$$

The series parametrized by the residues r_k and poles s_k is called the *oscillatory part* of g and the integral term is referred to as the *diffusive part* of g , defined by the diffusive weight μ . The diffusive part must satisfy the integrability condition (6b) for (5) to be mathematically meaningful. The growth condition is not detailed herein since the studied functions have a finite number of poles s_k (see Theorem 2.16 in [49] for a full description of the conditions).

This formulation represents a complex function with an infinite sum and a continuous superposition of first-order systems, which leads to an MM expression once the diffusive part has been discretized. Because of the fractional calculus tools [37] needed to express α and β with an OD representation, functions are defined in the complex plane with their analytic extension and appropriate cuts.

2.2.1 Diffusive representation of the dynamic tortuosity

The dynamic tortuosity (7) is expressed in the Laplace domain with its analytic extension in the left half-plane to find its diffusive representation. A definition of α on the whole complex plane would lead to a multivalued function, which is inconsistent with the complex analysis techniques used to find its diffusive representation. Hence, a cut on \mathbb{R}^- is chosen, leading to a single-valued dynamic tortuosity, which preserves hermitian symmetry.

$$\alpha(s) = \alpha_\infty \left[1 + \frac{M}{s} + N \frac{\sqrt{1 + \frac{s}{L}} - 1}{s} \right] \quad (s \in \mathbb{C} \setminus (-\infty, -L]), \quad (7)$$

where $M = \nu\phi/(k_0\alpha_\infty)$, $N = 2\nu/(\Lambda^2(\alpha_0/\alpha_\infty - 1))$ and $L = \nu/(\Lambda^2(\alpha_0/\alpha_\infty - 1)^2)$ are all positive real numbers. A necessary condition for (7) to admit an OD representation is to vanish when the norm of s tends to infinity, which is presently not the case as such. Consequently, the focus is solely on a part of α which contains the irrational terms and decays at infinity. Several parts of (7) admit an OD representation, but to avoid unnecessary calculations, the focus is on (8) below, which appears to be the same diffusive part as the Atalla and Sgard perforation model [6].

$$\alpha_d(s) := \frac{1}{N} \left[\frac{\alpha(s)}{\alpha_\infty} - 1 - \frac{M}{s} \right] = \frac{\sqrt{1 + \frac{s}{L}} - 1}{s} \quad (s \in \mathbb{C} \setminus (-\infty, -L]). \quad (8)$$

It has been shown in [52] that (8) has no singularities and admits the diffusive representation (9) with a positive real-valued diffusive weight μ_J satisfying the integrability condition (6b).

$$\alpha_d(s) = \int_L^\infty \frac{\mu_J(\xi)}{s + \xi} d\xi \quad (s \in \mathbb{C} \setminus (-\infty, -L]), \quad (9)$$

$$\text{where } \mu_J(\xi) := \frac{1}{\pi} \frac{\sqrt{\frac{\xi}{L} - 1}}{\xi} \quad (\xi \in [L, +\infty)). \quad (10)$$

Finally, the dynamic tortuosity can be written with a diffusive representation as follows:

$$\alpha(s) = \alpha_\infty \left[1 + \frac{M}{s} + N \int_L^\infty \frac{\mu_J(\xi)}{s + \xi} d\xi \right] \quad (\Re(s) > 0). \quad (11)$$

2.2.2 Oscillatory-diffusive representation of the dynamic compressibility

The same methodology used to find the expression (11) for α is applied to the normalized dynamic compressibility β . First, the latter is expressed in the Laplace domain with the positive parameters M' , N' and L' for the sake of clarity. The extension to the left complex half-plane is done with the cut $(-\infty, L'] \subset \mathbb{R}^-$, which keeps the normalized dynamic compressibility single-valued:

$$\beta(s) = \gamma - (\gamma - 1) \left[1 + \frac{M'}{s} + N' \frac{\sqrt{1 + \frac{s}{L'} - 1}}{s} \right]^{-1} \quad (s \in \mathbb{C} \setminus (-\infty, -L']), \quad (12)$$

where $M' = \nu\phi/(k'_0 \text{Pr})$, $N' = 2\nu/(\Lambda'^2(\alpha'_0 - 1))$ and $L' = \nu/(\Lambda'^2(\alpha'_0 - 1)^2 \text{Pr})$. Unlike the dynamic tortuosity, the portion of β which tends to zero when the modulus of s approaches infinity is not related to a known diffusive part of functions studied in the literature. Hence, an investigation is done to find if (13) admits an OD representation.

$$\beta_{\text{od}}(s) := \frac{\beta(s) - 1}{\gamma - 1} = \frac{N' \sqrt{1 + \frac{s}{L'} + M' - N'}}{s + N' \sqrt{1 + \frac{s}{L'} + M' - N'}} \quad (s \in \mathbb{C} \setminus (-\infty, -L']). \quad (13)$$

Its study leads to two different representations whether there exists $s \in \mathbb{C} \setminus (-\infty, -L']$ such that the denominator of (13) equals to zero or not. As fully detailed in A.1, the two cases can be distinguished by the sign of the quantity $M' - N' - L'$ and thus by the physical parameters. Herein, the conditions differentiating the two cases are also expressed through the static thermal tortuosity α'_0 which we recall that it satisfies $\alpha'_0 \geq 1$ by definition.

First case: $M' - N' - L' > 0$.

According to the definition of M' , N' and L' , the condition of having $M' - N' - L'$ positive implies:

$$\alpha'_0 > 1 + \frac{k'_0}{\phi\Lambda'^2} \left(1 + \sqrt{1 + \frac{\phi\Lambda'^2}{k'_0}} \right). \quad (14)$$

As proved in A.1, the denominator of β_{od} can never be zero in this case. Therefore, β_{od} simply admits a diffusive representation (15) with a diffusive weight (16), which is real-valued and positive (like μ_J), and yields a well-posed diffusive part.

$$\beta_{\text{od}}(s) = N' \int_{L'}^\infty \frac{\nu_J(\xi)}{s + \xi} d\xi \quad (s \in \mathbb{C} \setminus (-\infty, -L']), \quad (15)$$

$$\nu_J(\xi) := \frac{1}{\pi} \frac{\xi \sqrt{\frac{\xi}{L'} - 1}}{(\xi - M' + N')^2 + N'^2 \left(\frac{\xi}{L'} - 1 \right)} \quad (\xi \in [L', +\infty)). \quad (16)$$

Second case: $M' - N' - L' < 0$.

The condition of having $M' - N' - L'$ negative implies that

$$\alpha'_0 < 1 + \frac{k'_0}{\phi\Lambda'^2} \left(1 + \sqrt{1 + \frac{\phi\Lambda'^2}{k'_0}} \right). \quad (17)$$

In this case, β_{od} has the same diffusive part as in the first case. However, it also admits an oscillatory part consisting of one pole s_0 with weight r_0 . Indeed, if the relation (17) is fulfilled, then β_{od} has a unique negative singularity $s_0 \in [-L', 0[$ given by (85), with an associated positive residue r_0 given by (86). As a result, the function β_{od} can be recast as:

$$\beta_{\text{od}}(s) = \frac{r_0}{s - s_0} + N' \int_{L'}^{\infty} \frac{\nu_{\text{J}}(\xi)}{s + \xi} d\xi \quad (s \in \mathbb{C} \setminus (-\infty, -L']). \quad (18)$$

Finally, in both cases, the normalized dynamic compressibility can be recast with an OD representation:

$$\beta(s) = 1 + (\gamma - 1) \left[\frac{r_0}{s - s_0} + N' \int_{L'}^{\infty} \frac{\nu_{\text{J}}(\xi)}{s + \xi} d\xi \right] \quad (\Re(s) > 0), \quad (19)$$

where r_0 is taken null if $M' - N' - L'$ is positive.

The dynamic tortuosity and normalized dynamic compressibility of the JCAPL model can therefore be expressed with (11) and (19), respectively. These expressions do not contain irrational terms with s and appear like an MM with an infinite number of weights and poles. Hence, a discretization of their diffusive part leads straightforwardly to an MM.

2.3 Discussion on the diffusive representation for other models

Identical techniques can be applied to other models. In this section, the Wilson model [67, 68] and the Horoshenkov model [35, 36] are looked into in order to exhibit a diffusive representation which can be straightforwardly discretized as an MM.

The Wilson dynamic tortuosity can be linked to the JCAPL one with the proper definition of M , N and L (see Table 1). Moreover, the Wilson normalized dynamic compressibility can be expressed as follows:

$$\beta_{\text{w}}(s) = 1 + (\gamma - 1) \int_{\tau_e^{-1}}^{\infty} \frac{\nu_{\text{w}}(\xi)}{s + \xi} d\xi \quad (\Re(s) > 0), \quad (20)$$

where τ_e is the entropy-mode relaxation time. In contrast to the JCAPL model, the diffusive weight ν_{w} , whose expression is given by (92), is a negative function. However, another representation of β_{w} containing an extended diffusive representation can be used to obtain a diffusive weight $\tilde{\nu}_{\text{w}}$ that is always positive:

$$\beta_{\text{w}}(s) = (\gamma - 1) \int_{\tau_e^{-1}}^{\infty} \tilde{\nu}_{\text{w}}(\xi) \frac{1}{s + \xi} d\xi + (\gamma - 1) \tau_e \int_{\tau_e^{-1}}^{\infty} \tilde{\nu}_{\text{w}}(\xi) \frac{s}{s + \xi} d\xi \quad (\Re(s) > 0), \quad (21)$$

where $\tilde{\nu}_{\text{w}} \geq 0$ is given by (95) in A.2 with the steps leading to (21).

The Horoshenkov model gives an expression of α and β similar to the JCAPL model with a slightly different expression for the last terms that are in factor of N and N' in (7) and (12), respectively (a difference highlighted in A.3). Therefore, the Horoshenkov model cannot be linked in a straightforward manner to the JCAPL model, although we can show that it admits a similar diffusive representation regarding the dynamic tortuosity:

$$\alpha_{\text{h}}(s) = \alpha_{\infty} \left[1 + \frac{M_{\text{h}}}{s} + N_{\text{h}} \int_0^{\infty} \frac{\mu_{\text{h}}(\xi)}{s + \xi} d\xi \right] \quad (\Re(s) > 0), \quad (22)$$

$$\text{with } \mu_{\text{h}}(\xi) = \frac{1}{\pi} \frac{\sqrt{\frac{\xi}{L_{\text{h}}}}}{\frac{\xi}{L_{\text{h}}} + 1} \quad (\xi \in [0, +\infty)), \quad (23)$$

where $M_{\text{h}} = M = \nu\phi/(k_0\alpha_{\infty})$, $N_{\text{h}} = \theta_{\rho,1}$ and $L_{\text{h}} = M_{\text{h}}/\theta_{\rho,3}^2$. Here, the coefficients $\theta_{\rho,1}$ and $\theta_{\rho,3}$ are the Padé approximant parameters used in the Horoshenkov model [35, 36]. Compared to the JCAPL model, the Horoshenkov

model exhibits a diffusive part where $\xi = 0^+$ is reached, which induces a long-memory behaviour of the viscous dissipation in the time-domain. The same remark can be done for the Horoshenkov normalized dynamic compressibility (24), which is obtained by starting with a similar isolated term as in (13) and then by following the same approach as for the JCAPL model.

$$\beta_h(s) = 1 + (\gamma - 1) N'_h \int_0^\infty \frac{\nu_h(\xi)}{s + \xi} d\xi \quad (\Re(s) > 0), \quad (24)$$

where ν_h , given in A.3, is a positive function on \mathbb{R}^+ .

This section has gathered OD and diffusive representations of α and β described by different models. As mentioned before, the Wilson dynamic tortuosity can be described by the JCAPL dynamic tortuosity. Moreover, the JCAPL model is an extension of the JCAL and JCA models. Hence, with the right set of parameters, the expression of the dynamic tortuosity and normalized dynamic compressibility given by the JCAPL model can cover the JCAL and JCA models. The connections between these models are gathered in Table 1.

Table 1: Parameters of expressions (7) and (12) defining α and β given for several models, with the cross \times indicating the impossibility to describe the corresponding model with these expressions.

Variable	Parameter	JCAPL	JCAL	JCA	Wilson	Horoshenkov
α	M	$\frac{\nu\phi}{k_0\alpha_\infty}$	$\frac{\nu\phi}{k_0\alpha_\infty}$	$\frac{\nu\phi}{k_0\alpha_\infty}$	$\frac{2}{\tau_v}$	\times
	N	$\frac{2\nu}{\Lambda^2 \left(\frac{\alpha_0}{\alpha_\infty} - 1\right)}$	$\frac{\nu\phi}{k_0\alpha_\infty}$	$\frac{\nu\phi}{k_0\alpha_\infty}$	$\frac{1}{\tau_v}$	
	L	$\frac{\nu}{\Lambda^2 \left(\frac{\alpha_0}{\alpha_\infty} - 1\right)^2}$	$\frac{\nu\phi^2\Lambda^2}{4k_0^2\alpha_\infty^2}$	$\frac{\nu\phi^2\Lambda^2}{4k_0^2\alpha_\infty^2}$	$\frac{1}{\tau_v}$	
β	M'	$\frac{\nu\phi}{k'_0\text{Pr}}$	$\frac{\nu\phi}{k'_0\text{Pr}}$	$\frac{8\nu}{\Lambda'^2\text{Pr}}$	\times	\times
	N'	$\frac{2\nu}{\Lambda'^2(\alpha'_0 - 1)\text{Pr}}$	$\frac{\nu\phi}{k'_0\text{Pr}}$	$\frac{8\nu}{\Lambda'^2\text{Pr}}$		
	L'	$\frac{\nu}{\Lambda'^2(\alpha'_0 - 1)^2\text{Pr}}$	$\frac{\nu\phi^2\Lambda'^2}{4k_0'^2\text{Pr}}$	$\frac{16\nu}{\Lambda'^2\text{Pr}}$		

Note that for the JCA and JCAL dynamic compressibility, the inequality $M' - N' - L' < 0$ is always satisfied. Hence, β always admits an OD representation for these two models.

3 Stability analysis of the Johnson-Champoux-Allard-Pride-Lafarge equivalent fluid model

Based on diffusive representations, a stability analysis of the time-domain JCAPL-EFM is carried out thanks to an energy approach. An introduction to the diffusive realization used to express the time convolution products \star with a time-local representation is first given. The energy defined for the JCAPL-EFM is then presented, followed by a proof of the JCAPL-EFM stability. We refer to [46] for the definitions and properties lying behind the mathematical tools used in this section.

3.1 Extended diffusive realization

For a given transfer function \widehat{G} admitting a diffusive representation defined by a diffusive weight ν_G , the diffusive realization of \widehat{G} applied to a scalar time-dependent function p is:

$$\begin{cases} y_p(t, \mathbf{x}) := \int_0^\infty \nu_G(\xi) \psi(\xi; t, \mathbf{x}) d\xi, & (25) \\ \partial_t \psi(\xi; t, \mathbf{x}) = -\xi \psi(\xi; t, \mathbf{x}) + p(t, \mathbf{x}), \quad \psi(\xi; 0, \mathbf{x}) = 0. & (26) \end{cases}$$

The function p can be seen as an input of the convolution system $G \star p$, while the function $y_p = G \star p$ is the output, and the state ψ is called the diffusive variable. However, the JCAPL transfer functions, α and β , are applied to the time derivative of the velocity and pressure in the EFM. Hence, the desired diffusive realization makes use of $z_p := G \star \partial_t p$ as output. Such a realization is called an *extended* diffusive realization, and writes:

$$z_p(t, \mathbf{x}) := \int_0^\infty \nu_G(\xi) \partial_t \psi(\xi; t, \mathbf{x}) d\xi, \quad (27)$$

with ψ solution of (26). In addition, an energy functional can be defined for the extended diffusive realization:

$$E_\psi(t) := \frac{1}{2} \int_\Omega \int_0^\infty \nu_G(\xi) \xi |\psi(\xi; t, \mathbf{x})|^2 d\xi d\mathbf{x}, \quad (28)$$

the derivative of which is:

$$\frac{d}{dt} E_\psi(t) = \int_\Omega \int_0^\infty \nu_G(\xi) \xi \psi(\xi; t, \mathbf{x}) \partial_t \psi(\xi; t, \mathbf{x}) d\xi d\mathbf{x} \quad (29a)$$

$$= \int_\Omega \int_0^\infty \nu_G(\xi) [p(t, \mathbf{x}) - \partial_t \psi(\xi; t, \mathbf{x})] \partial_t \psi(\xi; t, \mathbf{x}) d\xi d\mathbf{x} \quad (29b)$$

$$= \int_\Omega p(t, \mathbf{x}) \left(\int_0^\infty \nu_G(\xi) \partial_t \psi(\xi; t, \mathbf{x}) d\xi \right) d\mathbf{x} - \int_\Omega \int_0^\infty \nu_G(\xi) (\partial_t \psi(\xi; t, \mathbf{x}))^2 d\xi d\mathbf{x} \quad (29c)$$

$$= \int_\Omega p(t, \mathbf{x}) z_p(t, \mathbf{x}) d\mathbf{x} - \int_\Omega \int_0^\infty \nu_G(\xi) (\partial_t \psi(\xi; t, \mathbf{x}))^2 d\xi d\mathbf{x}. \quad (29d)$$

Equation (26) is used to get (29b) from (29a). After some rearrangement, the last equation (29d) is obtained from (29c) by using (27). If the diffusive weight ν_G is a *positive* function, then the second term of the right-hand side of (29d) is always negative and a lossy power balance can be found for E_ψ :

$$\frac{d}{dt} E_\psi(t) \leq (p, z_p)_{L^2(\Omega)}, \quad (30)$$

where $(\cdot, \cdot)_{L^2(\Omega)}$ denotes L^2 -inner product.

The extension of scalar extended diffusive realizations to the vector-valued case is straightforward. Next, analogous equations to those obtained for p are presented below for a vector of functions \mathbf{u} , as it will be used for the velocity field in the stability analysis.

$$\begin{cases} \mathbf{z}_\mathbf{u}(t, \mathbf{x}) := \int_0^\infty \mu_G(\xi) \partial_t \boldsymbol{\phi}(\xi; t, \mathbf{x}) d\xi, \\ \partial_t \boldsymbol{\phi}(\xi; t, \mathbf{x}) = -\xi \boldsymbol{\phi}(\xi; t, \mathbf{x}) + \mathbf{u}(t, \mathbf{x}), \quad \boldsymbol{\phi}(\xi; 0, \mathbf{x}) = \mathbf{0}. \end{cases} \quad (31)$$

$$\quad (32)$$

The energy functional associated with (31)-(32) and its derivative are:

$$E_\boldsymbol{\phi}(t) := \frac{1}{2} \int_\Omega \int_0^\infty \mu_G(\xi) \xi \|\boldsymbol{\phi}(\xi; t, \mathbf{x})\|^2 d\xi d\mathbf{x}, \quad (33)$$

$$\frac{d}{dt} E_\boldsymbol{\phi}(t) = \int_\Omega \mathbf{u}(t, \mathbf{x}) \cdot \mathbf{z}_\mathbf{u}(t, \mathbf{x}) d\mathbf{x} - \int_\Omega \int_0^\infty \mu_G(\xi) \|\partial_t \boldsymbol{\phi}(\xi; t, \mathbf{x})\|^2 d\xi d\mathbf{x} \leq (\mathbf{u}, \mathbf{z}_\mathbf{u})_{L^2(\Omega; \mathbb{R}^2)}, \quad (34)$$

where $\|\cdot\|$ is the euclidian norm.

3.2 Energy balance

The JCAPL-EFM is first written in the Laplace domain (35) with the OD representations (11) and (19) of the dynamic variables. For the sake of clarity, spatial, time and Laplace variables are omitted for the velocity \mathbf{u} and

the pressure p .

$$\begin{cases} s \hat{\mathbf{u}} + M \hat{\mathbf{u}} + N \int_L^\infty \mu_J(\xi) \frac{s \hat{\mathbf{u}}}{s + \xi} d\xi = -\frac{1}{\rho_0 \alpha_\infty} \nabla \hat{p}, \\ s \hat{p} + (\gamma - 1) r_0 \frac{s \hat{p}}{s - s_0} + (\gamma - 1) N' \int_{L'}^\infty \nu_J(\xi) \frac{s \hat{p}}{s + \xi} d\xi = -\frac{1}{\chi_0} \nabla \cdot \hat{\mathbf{u}}. \end{cases} \quad (35)$$

To express system (35) in the time domain, extended diffusive realizations are used for the diffusive part of both equations with the vector-valued diffusive variable ϕ and the scalar diffusive variable ψ used for the velocity \mathbf{u} and the pressure p , respectively. Therefore, the term $s \hat{\mathbf{u}}/(s + \xi)$ (resp. $s \hat{p}/(s + \xi)$) in (35) are the Laplace transforms of $\partial_t \phi$ (resp. $\partial_t \psi$), which is straightforward to verify from (32) (resp. (26)). Moreover, non-null initial conditions are set for the diffusive variables to regularize the extended diffusive realization at $t = 0$ [43]. Indeed, they correspond to null initial conditions for the time derivative of the diffusive variables, which is needed for the integrals of (36a) and (36b) to be finite at $t = 0$.

$$\begin{cases} \partial_t \mathbf{u} + M \mathbf{u} + N \int_L^\infty \mu_J(\xi) \partial_t \phi(\xi; t, \mathbf{x}) d\xi = -\frac{1}{\rho_0 \alpha_\infty} \nabla p, \end{cases} \quad (36a)$$

$$\begin{cases} \partial_t p + (\gamma - 1) r_0 \partial_t \psi(-s_0; t, \mathbf{x}) + (\gamma - 1) N' \int_{L'}^\infty \nu_J(\xi) \partial_t \psi(\xi; t, \mathbf{x}) d\xi = -\frac{1}{\chi_0} \nabla \cdot \mathbf{u}, \end{cases} \quad (36b)$$

$$\begin{cases} \partial_t \phi(\xi; t, \mathbf{x}) = -\xi \phi(\xi; t, \mathbf{x}) + \mathbf{u}, \end{cases} \quad (36c)$$

$$\begin{cases} \partial_t \psi(\xi; t, \mathbf{x}) = -\xi \psi(\xi; t, \mathbf{x}) + p, \end{cases} \quad (36d)$$

$$\begin{cases} \phi(\xi; 0, \mathbf{x}) = \mathbf{u}(0, \mathbf{x})/\xi, \end{cases} \quad (36e)$$

$$\begin{cases} \psi(\xi; 0, \mathbf{x}) = p(0, \mathbf{x})/\xi. \end{cases} \quad (36f)$$

A particular feature appears in equation (36b), where an additional term with the diffusive variable ψ can exist for an isolated point at $\xi = -s_0 \geq 0$, associated with a fixed weight $r_0 \geq 0$ (as previously explained in Section 2.2.2). Although it is separated from the diffusive representation in the third term of (36b), it is solution of the same auxiliary equation (36d).

The classical mechanical energy is defined below, divided into a kinetic energy and a potential energy:

$$E_m(t) := \frac{\rho_0 \alpha_\infty}{2} \int_\Omega \|\mathbf{u}\|^2 d\mathbf{x} + \frac{\chi_0}{2} \int_\Omega p^2 d\mathbf{x}. \quad (37)$$

Additionally, based on (28) and (33) with the diffusive weights $\mu_G = \mu_J$ and $\nu_G = \nu_J$ (defined in (10) and (16), respectively), a *diffusive* energy is defined as a linear combination of the energy associated with each diffusive variables:

$$E_{\text{diff}}(t) := \rho_0 \alpha_\infty N E_\phi(t) + \chi_0 (\gamma - 1) N' E_\psi(t) + \chi_0 (\gamma - 1) E_{\psi_0}(t), \quad (38)$$

with E_{ψ_0} the energy associated with the diffusive variable ψ evaluated at $\xi = -s_0$, defined in (39). Therefore, it is very similar to E_ψ given in (28) with the residue r_0 playing the role of a constant diffusive weight.

$$E_{\psi_0}(t) := \int_\Omega r_0 (-s_0) |\psi(-s_0; t, \mathbf{x})|^2 d\mathbf{x}. \quad (39)$$

It is important to recall that in (39), $r_0 \geq 0$ and $s_0 \leq 0$, and thus E_{diff} is positive-definite. The global energy functional associated with the extended dynamical system (36) with $(\mathbf{u}, p, \phi, \psi)$ as state variables is defined below:

$$\mathcal{E}(t) := E_m(t) + E_{\text{diff}}(t), \quad (40)$$

$$\begin{aligned} &= \frac{\rho_0 \alpha_\infty}{2} \left(\int_\Omega \|\mathbf{u}\|^2 d\mathbf{x} + N \int_\Omega \int_L^\infty \mu_J(\xi) \xi \|\phi(\xi; t, \mathbf{x})\|^2 d\xi d\mathbf{x} \right) + \\ &\quad \frac{\chi_0}{2} \left(\int_\Omega p^2 d\mathbf{x} + (\gamma - 1) N' \int_\Omega \int_{L'}^\infty \nu_J(\xi) \xi |\psi(\xi; t, \mathbf{x})|^2 d\xi d\mathbf{x} + (\gamma - 1) \int_\Omega r_0 (-s_0) |\psi(-s_0; t, \mathbf{x})|^2 d\mathbf{x} \right). \end{aligned}$$

Note that the positivity of the JCPL diffusive weights μ_J and ν_J enables to prove the positive-definiteness of \mathcal{E} . It is also a key aspect of the following proposition.

Proposition 3.1. *In a bounded domain Ω with no contribution at the boundary (either $p = 0$, or $\mathbf{u} \cdot \mathbf{n} = 0$ on $\partial\Omega$), the augmented energy \mathcal{E} of the JCAPL-EFM satisfies:*

$$\frac{d}{dt}\mathcal{E}(t) = -\rho_0 \alpha_\infty M \int_{\Omega} \|\mathbf{u}\|^2 d\mathbf{x} - \rho_0 \alpha_\infty N \int_{\Omega} \int_L^\infty \mu_J(\xi) \|\partial_t \boldsymbol{\phi}(\xi)\|^2 d\xi d\mathbf{x} \quad (41a)$$

$$- \chi_0 (\gamma - 1) N' \int_{\Omega} \int_{L'}^\infty \nu_J(\xi) (\partial_t \psi(\xi))^2 d\xi d\mathbf{x} - \chi_0 (\gamma - 1) \int_{\Omega} r_0 (\partial_t \psi(-s_0))^2 d\xi d\mathbf{x}, \quad (41b)$$

$$\leq 0. \quad (41c)$$

Hence, the augmented energy \mathcal{E} is decreasing. Moreover, the dynamical system proves to be asymptotically stable, i.e. $(\mathbf{u}, p, \boldsymbol{\phi}, \psi) \rightarrow (\mathbf{0}, 0, \mathbf{0}, 0)$ as $t \rightarrow \infty$ in the appropriate energy space.

Proof. (sketch of)

Let us first compute separately the derivative of the mechanical energy and the derivative of the energy associated with the diffusive variables. In order to keep the proof readable, the time and spatial variables are omitted for all functions.

- The derivative of the mechanical energy is first tackled. In the following calculations, equations (36a) and (36b) are used to replace the spatial derivatives of \mathbf{u} and p appearing in the first equality.

$$\frac{d}{dt}E_m(t) = \rho_0 \alpha_\infty \int_{\Omega} \mathbf{u} \cdot \partial_t \mathbf{u} d\mathbf{x} + \chi_0 \int_{\Omega} p \partial_t p d\mathbf{x}, \quad (42a)$$

$$= - \int_{\partial\Omega} p \mathbf{u} \cdot \mathbf{n} d\sigma - \rho_0 \alpha_\infty M \int_{\Omega} \|\mathbf{u}\|^2 d\mathbf{x} - \rho_0 \alpha_\infty N \int_{\Omega} \int_L^\infty \mu_J(\xi) \mathbf{u} \cdot \partial_t \boldsymbol{\phi}(\xi) d\xi d\mathbf{x} \quad (42b)$$

$$- \chi_0 (\gamma - 1) N' \int_{\Omega} \int_{L'}^\infty \nu_J(\xi) p \partial_t \psi(\xi) d\xi d\mathbf{x} - \chi_0 (\gamma - 1) \int_{\Omega} r_0 p \partial_t \psi(-s_0) d\mathbf{x}, \quad (42c)$$

$$= - \rho_0 \alpha_\infty M \int_{\Omega} \|\mathbf{u}\|^2 d\mathbf{x} - \rho_0 \alpha_\infty N \int_{\Omega} \mathbf{u} \cdot \mathbf{z}_u d\mathbf{x} - \chi_0 (\gamma - 1) N' \int_{\Omega} p z_p d\mathbf{x} - \chi_0 (\gamma - 1) r_0 \int_{\Omega} p \partial_t \psi(-s_0) d\mathbf{x}. \quad (42d)$$

The integral on $\partial\Omega$ in (42b) stands for the classical interaction with the exterior of Ω , and is equal to zero when either $p = 0$ or $\mathbf{u} \cdot \mathbf{n} = 0$ at the boundary. Moreover, \mathbf{z}_u and z_p are defined as in (31) and (27), respectively, with the positive diffusive weights $\mu_G = \mu_J$ and $\nu_G = \nu_J$. Note that the first term of equality (42d) is negative, while the others do not have a definite sign.

- The derivative of the energy resulting from the auxiliary variables is now addressed. The previous expressions (29d) and (34) of the derivatives of the energy defined for the extended diffusive realization is used in the next calculations, with the same \mathbf{z}_u and z_p used for the mechanical energy.

$$\frac{d}{dt}E_{\text{diff}}(t) = \rho_0 \alpha_\infty N \frac{d}{dt}E_{\boldsymbol{\phi}}(t) + \chi_0 (\gamma - 1) N' \frac{d}{dt}E_{\psi}(t) - \chi_0 (\gamma - 1) \frac{d}{dt}E_{\psi_0}(t), \quad (43a)$$

$$= - \rho_0 \alpha_\infty N \int_{\Omega} \int_L^\infty \mu_J(\xi) \|\partial_t \boldsymbol{\phi}(\xi)\|^2 d\xi d\mathbf{x} + \rho_0 \alpha_\infty N \int_{\Omega} \mathbf{u} \cdot \mathbf{z}_u d\mathbf{x} \quad (43b)$$

$$- \chi_0 (\gamma - 1) N' \int_{\Omega} \int_{L'}^\infty \nu_J(\xi) (\partial_t \psi(\xi))^2 d\xi d\mathbf{x} + \chi_0 (\gamma - 1) N' \int_{\Omega} p z_p d\mathbf{x} \quad (43c)$$

$$- \chi_0 (\gamma - 1) \int_{\Omega} r_0 (\partial_t \psi(-s_0))^2 d\xi d\mathbf{x} + \chi_0 (\gamma - 1) \int_{\Omega} r_0 p \partial_t \psi(-s_0) d\mathbf{x}. \quad (43d)$$

The last term of (43a) is handled with the same approach used in (29), i.e. using (26) to rewrite the term $-s_0 \psi(-s_0)$. The weight r_0 and the diffusive weights μ_J and ν_J are known to be positive, therefore, the first terms of (43b),

(43c) and (43d) are negative. However, the last term of each of these three lines does not have a known sign, but it is always the opposite of the one found in (42d).

• Let us now focus on the global energy \mathcal{E} , and more particularly on the sign-varying terms in E_m and E_{diff} . Summing up relations (42d) and (43), respectively, leads to the cancelling of the last three terms of (42d) by the last term of (43b), (43c) and (43d), respectively. Consequently, the only remaining terms in the derivative of the augmented energy \mathcal{E} are all negative:

$$\frac{d}{dt}\mathcal{E}(t) = \frac{d}{dt}E_m(t) + \frac{d}{dt}E_{\text{diff}}(t), \quad (44a)$$

$$= -\rho_0 \alpha_\infty M \int_{\Omega} \|\mathbf{u}\|^2 d\mathbf{x} - \rho_0 \alpha_\infty N \int_{\Omega} \int_L^\infty \mu_J(\xi) \|\partial_t \phi(\xi)\|^2 d\xi d\mathbf{x} \quad (44b)$$

$$- \chi_0 (\gamma - 1) N' \int_{\Omega} \int_{L'}^\infty \nu_J(\xi) (\partial_t \psi(\xi))^2 d\xi d\mathbf{x} - \chi_0 (\gamma - 1) \int_{\Omega} r_0 (\partial_t \psi(-s_0))^2 d\xi d\mathbf{x}, \quad (44c)$$

$$\leq 0. \quad (44d)$$

Assuming that functions are defined in some appropriate functional spaces, relation (40) implies the *stability* of the JCAPL-EFM, i.e. $\mathcal{E}(t) \leq \mathcal{E}(t=0)$; care must be taken that since pressure p is defined up to an additive constant, the appropriate functional space will include the zero mean pressure $\int_{\Omega} p d\mathbf{x} = 0$ as a constraint. Moreover, following results from [47], [50] and references therein, the *asymptotic stability* of the augmented system can be proved: it means that all the components of the augmented state vector $(\mathbf{u}, p, \phi, \psi)$ tend to zero in the appropriate energy space, as t tends to infinity. \square

A similar global energy functional can be defined with the diffusive representation of the Horoshenkov model. The diffusive weights (23) and (100) being positive, the same conclusion is drawn: the Horoshenkov model is stable. However, despite the positive diffusive weights obtained for the Wilson model, the extended diffusive representation in β_w prevents one from applying the same methodology. In fact, a second-order derivative appears when multiplying β_w by the derivative of p . In order to work with the functional spaces needed for the proof of stability based on diffusive representations, an extended diffusive representation applied to the derivative of the input p can be used for the Wilson-EFM. However, this formulation does not lead to an energy balance where terms without definite sign cancel each other as in the JCAPL-EFM. Hence, no conclusion can be drawn for the stability of the Wilson-EFM.

4 Equivalent fluid model based on multipole model

An approximated model for the EFM using an MM to describe α and β is proposed in this section. An investigation is done on the multipole-based EFM to find sufficient conditions depending on the MM parameters to ensure its stability.

4.1 Multipole model approximation

The dynamic tortuosity and normalized dynamic compressibility can be recast in the Laplace domain with a continuous superposition of first-order systems. This result, shown in Section 2 for several models, justifies an approximation of these quantities for numerical modeling by a finite number of first-order system, namely an MM. Consequently, α and β are chosen to be approximated by the complex functions α_{mm} and β_{mm} defined by:

$$\alpha_{\text{mm}}(s) = c_0 + \frac{c_{-1}}{s} + \sum_{k=1}^K \frac{r_k}{s - s_k}, \quad (45)$$

$$\beta_{\text{mm}}(s) = c'_0 + \frac{c'_{-1}}{s} + \sum_{k=1}^{K'} \frac{r'_k}{s - s'_k}. \quad (46)$$

The coefficients c_0 , c_{-1} , c'_0 and c'_{-1} are obtained from the asymptotic behaviour of α and β . Hence, one obtains in a straightforward manner that $c_0 = \alpha_\infty$, $c_{-1} = \nu\phi/k_0 = \alpha_\infty M$, $c'_0 = 1$ and $c'_{-1} = 0$. However, they are not replaced by their value in this section in order to keep a symmetric form of the equations facilitating the reading. The weights r_k and r'_k and the poles s_k and s'_k are the parameters interpreted as the MM degrees of freedom, computed

with optimization approaches or quadrature methods. In a general MM, these parameters can be complex, going by conjugate pairs when the MM satisfies the reality condition ($g(s) \in \mathbb{R}_+$ for $s \in \mathbb{R}^+$). Herein, the parameters r_k, r'_k, s_k and s'_k are assumed real due to the OD representations of α and β . Indeed, these representations have a real-valued diffusive weight and the possible oscillatory part in the JCAPL normalized dynamic compressibility is described by real parameters too. This choice matches the approximations of the Biot-JKD equations [14, 55]. Moreover, the latest numerical studies based on MMs for wave propagation in conventional porous media with only a dissipative nature [4, 72] use real parameters, which is consistent with the previous section.

By injecting (45) and (46) into the EFM equations (1) and by using the original strategy brought out in [69], which consists in using the partial fraction decomposition

$$\frac{s}{s - s_k} = 1 + \frac{s_k}{s - s_k}, \quad (47)$$

the following system is obtained:

$$\begin{cases} s \hat{\mathbf{u}} + \left(\frac{c_{-1}}{c_0} + \sum_{k=1}^K \frac{r_k}{c_0} \right) \hat{\mathbf{u}} + \sum_{k=1}^K \frac{r_k s_k}{c_0} \frac{1}{s - s_k} \hat{\mathbf{u}} = -\frac{1}{\rho_0 c_0} \nabla \hat{p}, \\ s \hat{p} + \left(\frac{c'_{-1}}{c'_0} + \sum_{k=1}^{K'} \frac{r'_k}{c'_0} \right) \hat{p} + \sum_{k=1}^{K'} \frac{r'_k s'_k}{c'_0} \frac{1}{s - s'_k} \hat{p} = -\frac{1}{\chi_0 c'_0} \nabla \cdot \hat{\mathbf{u}}. \end{cases} \quad (48)$$

The ADE method [25] is applied on (48), describing the set of equations in the time-domain with causal convolutions computed through the auxiliary functions $\phi_{\mathbf{k}}$ and ψ_k .

$$\begin{cases} \partial_t \mathbf{u} + \frac{1}{\rho_0 c_0} \nabla p + \left(\frac{c_{-1}}{c_0} + \sum_{k=1}^K \frac{r_k}{c_0} \right) \mathbf{u} + \sum_{k=1}^K \frac{r_k s_k}{c_0} \phi_{\mathbf{k}} = 0, \end{cases} \quad (49a)$$

$$\begin{cases} \partial_t p + \frac{1}{\chi_0 c'_0} \nabla \cdot \mathbf{u} + \left(\frac{c'_{-1}}{c'_0} + \sum_{k=1}^{K'} \frac{r'_k}{c'_0} \right) p + \sum_{k=1}^{K'} \frac{r'_k s'_k}{c'_0} \psi_k = 0, \end{cases} \quad (49b)$$

$$\begin{cases} \partial_t \phi_{\mathbf{k}} = s_k \phi_{\mathbf{k}} + \mathbf{u} \end{cases} \quad (\forall k \in \llbracket 1, K \rrbracket), \quad (49c)$$

$$\begin{cases} \partial_t \psi_k = s'_k \psi_k + p \end{cases} \quad (\forall k \in \llbracket 1, K' \rrbracket). \quad (49d)$$

The additional initial conditions needed for the auxiliary functions depend on the principal variables

$$\phi_{\mathbf{k}}(0, \mathbf{x}) = -\mathbf{u}(0, \mathbf{x}) / s_k, \quad (50)$$

$$\psi_k(0, \mathbf{x}) = -p(0, \mathbf{x}) / s'_k, \quad (51)$$

mimicking the general initial conditions (36e) and (36f), although in practice, the initial pressure and velocity fields in a porous media are null.

Thanks to the partial fraction decomposition (47) done before applying the inverse Laplace transform, there is no spatial derivative in the additional equations (49c) and (49d). Hence, when the system is discretized with a numerical scheme based on fluxes, these fluxes depend on the velocity and pressure, but not on the auxiliary variables. Consequently, the problem to solve at each mesh interface does not grow with the number of additional variables. Moreover, for problems with multiple subdomains, there are no additional fluxes to manage at the interface between them.

4.2 Stability analysis

In section 3, the stability of the JCAPL-EFM was proved. Consequently, the approximated EFM should be built in such a way to keep the same stability property. Therefore, a stability analysis of the multipole-based EFM is performed in order to find sufficient conditions to ensure its stability. It is performed through the energy functional (52) defined analogously to the JCAPL-EFM global energy \mathcal{E} given equation (40). Here, the energy functional \mathcal{E}_a

can be seen as an approximation of \mathcal{E} with a discrete sum of diffusive variables.

$$\mathcal{E}_a(t) = \frac{\rho_0}{2} \left(c_0 \int_{\Omega} \|\mathbf{u}\|^2 \, d\mathbf{x} + \sum_{k=1}^K \int_{\Omega} r_k (-s_k) \|\phi_{\mathbf{k}}\|^2 \, d\mathbf{x} \right) + \frac{\chi_0}{2} \left(c'_0 \int_{\Omega} p^2 \, d\mathbf{x} + \sum_{k=1}^{K'} \int_{\Omega} r'_k (-s'_k) |\psi_k|^2 \, d\mathbf{x} \right), \quad (52)$$

whose derivative is:

$$\begin{aligned} \frac{d}{dt} \mathcal{E}_a(t) = & -\rho_0 c_{-1} \int_{\Omega} \|\mathbf{u}\|^2 \, d\mathbf{x} - \chi_0 c'_{-1} \int_{\Omega} p^2 \, d\mathbf{x} - \int_{\partial\Omega} p \mathbf{u} \cdot \mathbf{n} \, d\sigma \\ & -\rho_0 \sum_{k=1}^K r_k \int_{\Omega} \|\partial_t \phi_{\mathbf{k}}\|^2 \, d\mathbf{x} - \chi_0 \sum_{k=1}^{K'} r'_k \int_{\Omega} (\partial_t \psi_k)^2 \, d\mathbf{x}. \end{aligned} \quad (53)$$

From these last two equations, combined with the fact that ρ_0 , χ_0 , c_0 , c_{-1} , c'_0 and c'_{-1} are necessarily positive or null for conventional porous materials, the stability of the multipole-based EFM can be ensured under two sufficient conditions summarized in lemma 4.1.

Lemma 4.1. *In a bounded domain Ω with no contribution at the boundary (either $p = 0$, or $\mathbf{u} \cdot \mathbf{n} = 0$ on $\partial\Omega$), the approximated augmented energy \mathcal{E}_a is positive-definite and decreasing under the conditions:*

$$- \text{the poles } (s_k, s'_k)_k \text{ are negative real numbers,} \quad (C_1)$$

$$- \text{the weights } (r_k, r'_k)_k \text{ are positive real numbers.} \quad (C_2)$$

As a result, if (C_1) and (C_2) are fulfilled, then the multipole-based EFM is stable. It should be pointed out that the first condition (C_1) , which is extended for complex parameters by having the real part of the poles negative, is a necessary condition to have stable solutions. The methods used in the literature for wave propagation in porous media [4, 14, 69, 71] already satisfy this condition. The second condition (C_2) is analogous to the positivity of the JCAPL diffusive weights μ_J and ν_J needed to prove its stability. It is also similar to the stability conditions given by Blanc *et al.* [13] for the Biot-DA model.

5 Numerical implementation

In the following, two numerical studies are carried out. An energy analysis is first conducted in Section 5.2 on the discretized equations with a *toy model*. A more involved numerical analysis is then performed in Section 5.3, where a numerical porous material of realistic intrinsic properties placed in a 2D simulation mimicking an impedance tube experiment is considered. Prior to that, the numerical scheme is introduced. The choice made in this work is to use a fourth-order Runge-Kutta scheme [65] for the discretization in time. The space discretization is handled by a Discontinuous Galerkin (DG) scheme, a method well suited for acoustic problems [22].

5.1 Numerical scheme

Based on the theoretical results given in Sections 3 and 4 on the JCAPL-EFM stability and the multipole-based approximation, a numerical scheme is built to solve the augmented system (49). The system is rewritten below in hyperbolic form:

$$\partial_t \mathbf{q} + A_x \partial_x \mathbf{q} + A_y \partial_y \mathbf{q} + B \mathbf{q} = \mathbf{S}, \quad (54)$$

with the state variables $\mathbf{q} = (u \ v \ p \ \phi_1^X \ \dots \ \phi_K^X \ \phi_1^Y \ \dots \ \phi_K^Y \ \psi_1 \ \dots \ \psi_{K'})^T$. The auxiliary variables ϕ_k^X and ϕ_k^Y are associated with the two velocity components u and v , respectively, and ψ_k are the auxiliary variables associated with p . The vector \mathbf{S} is the source term and the Jacobian matrices A_x and A_y are defined as:

$$A_x = \left(\begin{array}{cccccccc} 0 & 0 & \frac{1}{\rho_0 c_0} & 0 & \dots & 0 \\ 0 & 0 & 0 & 0 & \dots & 0 \\ \frac{1}{\chi_0 c'_0} & 0 & 0 & 0 & \dots & 0 \\ 0 & 0 & 0 & 0 & \dots & 0 \\ \vdots & \vdots & \vdots & \vdots & \ddots & \vdots \\ 0 & 0 & 0 & 0 & \dots & 0 \end{array} \right), \quad A_y = \left(\begin{array}{cccccccc} 0 & 0 & 0 & 0 & \dots & 0 \\ 0 & 0 & \frac{1}{\rho_0 c_0} & 0 & \dots & 0 \\ 0 & \frac{1}{\chi_0 c'_0} & 0 & 0 & \dots & 0 \\ 0 & 0 & 0 & 0 & \dots & 0 \\ \vdots & \vdots & \vdots & \vdots & \ddots & \vdots \\ 0 & 0 & 0 & 0 & \dots & 0 \end{array} \right) \left. \begin{array}{l} \right\} (u, v, p) \\ \left. \right\} (\phi_k^X, \phi_k^Y, \psi_k) \end{array}, \quad (55)$$

where c_0 and c'_0 are some MM parameters, see equations (45) and (46). The relaxation matrix B is detailed in B, equation (101), and is in charge of the coupling between the auxiliary variables and the principal ones.

As noticed in [69], the advantage of (49), obtained in this format thanks to (47), is the absence of the auxiliary variables in the numerical flux used for the communication between the DG cells. As detailed in B, the time-domain system obtained without using the partial fractional decomposition (47) has different Jacobian matrices \widetilde{A}_x and \widetilde{A}_y in which lines associated with ϕ_k^X , ϕ_k^Y and ψ_k have non-null terms (see equation (106)). This is similar to other implementations [14, 26] where the auxiliary equations contain time or spatial derivatives of the principal variables. In the latter cases, when the number of auxiliary variables grows, the numerical cost increases more than for problems where no numerical flux is associated with the auxiliary equations.

5.1.1 Space discretization

Let $\Omega \subset \mathbb{R}^2$ be the computational domain for which there is a partition (\mathcal{T}_h) where h denotes the maximal diameter of the partition elements. The approximation space is taken as $V_h := \{v \mid \forall T \in \mathcal{T}_h, v|_T \in \mathbb{P}^k(T)\}$ where $\mathbb{P}^k(T)$ is the space of polynomials of degree at most k . A basis $\{\lambda_j^i \in \mathbb{P}^k(T_i), j = 1 \dots d\}$ with $d = (k+1)(k+2)/2$ is defined for each element $T_i \in \mathcal{T}_h$. Hence, a scalar function q is approximated on a cell T_i by:

$$q_h(\mathbf{x}, t) := \sum_{j=1}^d q_h^{i,j}(t) \lambda_j^i(\mathbf{x}). \quad (56)$$

Based on (56), the vector of solutions $\mathbf{q}_h(\mathbf{x}, t) = (u_h \ v_h \ p_h)$ is defined. Applying the DG method [34] results in:

$$\frac{d}{dt} \int_{T_i} \mathbf{q}_h(\mathbf{x}, t) \lambda_j^i d\Omega + \int_{T_i} \mathbf{F}(\mathbf{q}_h(\mathbf{x}, t)) \cdot \nabla \lambda_j^i d\Omega - \int_{\partial T_i} \mathbf{F}^*(\mathbf{q}_h^e(\mathbf{x}, t), \mathbf{q}_h^i(\mathbf{x}, t)) \cdot \mathbf{n}_i \lambda_j^i d\sigma + \int_{T_i} \mathbf{b}(\mathbf{q}_h(\mathbf{x}, t)) \lambda_j^i d\Omega = 0, \quad (57)$$

where $\mathbf{F}(q_h) = (A_x \mathbf{q}_h, A_y \mathbf{q}_h)$, $\mathbf{b}(\mathbf{q}_h) = B \mathbf{q}_h$, $\mathbf{n}^i = (n_x^i, n_y^i)$ is the outward unit normal to the edge ∂T_i and \mathbf{F}^* is the numerical flux. The solution \mathbf{q}_h on the edge of a cell T_i is denoted \mathbf{q}_h^i or \mathbf{q}_h^e when the interior or the exterior value of T is taken, respectively. In this work, the numerical flux used is the vector splitting

$$\mathbf{F}^*(\mathbf{q}_h^i, \mathbf{q}_h^e) = A^+ \mathbf{q}_h^i + A^- \mathbf{q}_h^e, \quad (58)$$

where incoming waves and outgoing waves are separated in A^+ and A^- . The latter contain respectively the positive eigenvalues and the negative eigenvalues of $A = A_x n_x + A_y n_y$. This flux solves exactly the monodimensional Riemann problem with constant coefficients. Note that for the boundary $\partial\Omega$, the centered flux

$$\mathbf{F}_{BC}^*(\mathbf{q}_h^i, \mathbf{q}_h^e) := A \frac{\mathbf{q}_h^i + \mathbf{q}_h^e}{2}, \quad (59)$$

is enforced with \mathbf{q}_h^e representing a ghost state defined with \mathbf{q}_h^i . Finally, the semi-discrete equation reads:

$$M \frac{d\mathbf{Q}_h}{dt}(t) := K \mathbf{Q}_h(t) + \widetilde{\mathbf{S}}(t), \quad (60)$$

where \mathbf{Q}_h is the unknown and $\widetilde{\mathbf{S}}$ is the source term.

5.1.2 Time discretization

The inversion of the mass matrix M in (60) is straightforward thanks to its block diagonal structure where each block is small enough to compute its inverse straightforwardly. Hence, the space discretization (60) can be rewritten

$$\frac{d\mathbf{Q}_h}{dt}(t) = \mathbf{L}_h(t, \mathbf{Q}_h(t)) = D \mathbf{Q}_h(t) + \mathbf{G}(t), \quad (61)$$

with \mathbf{L}_h the semi-discrete operator, $D = M^{-1}K$ and $\mathbf{G} = M^{-1}\widetilde{\mathbf{S}}$. The RKF84 eight-stage fourth-order 2N-storage Runge–Kutta method [65] is used for the time discretization as in [51]. It has been shown to be very efficient when combined with a DG space discretization for wave propagation problems.

Let $\{t^n\}_{n=0}^N$ be a partition of $[0, T] \subset \mathbb{R}^+$, $\Delta t = t^{n+1} - t^n$ the time step and \mathbf{Q}_h^n the approximated solution at time t^n . The steps of the RKF84 algorithms are

$$\mathbf{q}^{(0)} = \mathbf{Q}_h^n, \quad (62a)$$

$$d\mathbf{q}^{(i)} = A_i d\mathbf{q}^{(i-1)} + \mathbf{L}_h \left(t_n + c_i \Delta t, \mathbf{q}^{(i-1)} \right), \quad (62b)$$

$$\mathbf{q}^{(i)} = \mathbf{q}^{(i-1)} + B_i d\mathbf{q}^{(i)}, \quad \text{for } i = 1 \dots 8, \quad (62c)$$

$$\mathbf{Q}_h^{n+1} = \mathbf{q}^{(8)}, \quad (62d)$$

where the coefficients A_i , B_i and c_i are given Table A.9 in [65].

The stability condition for a scalar equation $\frac{dq}{dt} = dq$ writes:

$$|\Re(z)| \leq 1, \quad (63)$$

where $\Re(z) = q^{n+1}/q^n$ and $z = d \Delta t$. The stability condition can also be expressed with the Courant number C as:

$$C = d_m \frac{\Delta t}{h} \leq C^*, \quad (64)$$

with d_m the spectral radius of D and C^* the maximal Courant number given in [65] for different wavenumber and element size h in 1D. Consequently, the stability condition depends on the time and space discretization, the advection velocity, and on the poles present in the auxiliary equations. The latter could penalize the stability condition, especially at high frequencies where higher poles (in absolute value) are needed to accurately fit the dynamic variables. To circumvent this problem, another approach based on the splitting method [43] can be used, making the stability condition independent of the poles by resolving the ADE exactly. However, the range of frequencies studied in the numerical simulations herein does not involve poles that are significantly impacting the stability condition.

5.2 Energy analysis

The toy model studied in this section is built with MMs for α and β described by negative poles and different sets of weights. The weights are varied to explore cases where the stability condition (C_2) is fulfilled or not, in order to highlight the influence of the weights' sign.

5.2.1 Multipole-model parameters

The approximated EFM (54) is first solved for $\alpha_{\text{mm}}(s) = 1$ and $\beta_{\text{mm}}(s) = 1$, a case describing a medium without dissipative acoustic properties. In that case, $c_0 = c'_0 = 1$, $c_{-1} = c'_{-1} = 0$ and no pole is used (and therefore no auxiliary function). Then, we keep $\alpha_{\text{mm}}(s) = 1$ and we consider 3 different multipole-based approximations of:

$$\beta_{\text{toy}}(s) := 1 + \frac{\sqrt{s+2}}{s+1}, \quad (65)$$

which is a simplified model of β_{od} given in (19). Indeed, β_{toy} can be decomposed as a sum of a single-pole term and a diffusive part: $\beta_{\text{toy}}(s) = 1 + 1/(s+1) + \int_{L'=2}^{\infty} \nu_{\text{toy}}(\xi)/(s+\xi) d\xi$ with $\nu_{\text{toy}}(\xi) = \sqrt{\xi-2}/(\xi-1) \geq 0$. The positive diffusive weight and the positive residue of the single pole make clear that β_{toy} is a passive transfer function, namely $\Re(\beta_{\text{toy}}(s)) \geq 0$ for $\Re(s) \geq 0$. However, the multipole-based approximation does not take into account the known oscillatory-diffusive representation of β_{toy} in order to adopt a general approach where no analytical studies have been done before. Therefore, the multipole-based approximation is built from expression (65).

The MMs consist of a maximum of 4 poles and weights computed via the vector fitting algorithm [30] in order to fit β_{toy} over the frequency range [0.1Hz, 100Hz]. The constraint of 8 parameters is chosen arbitrarily in order to work with a small number of poles and weights. All the MM parameters are gathered in Table 2 with the non-dissipative case labeled as "Case 0". The Bode diagram comparing the MMs, with the reference function β_{toy} is shown in Fig. 1.

Table 2: Parameters of the multipole toy models associated with the 4 studied cases. The bold values are chosen arbitrarily while the other obtained with the vector fitting are rounded to two decimals places.

	Constants		Weights				Poles				Condition (C_2)
	c'_0	c'_{-1}	r'_0	r'_1	r'_2	r'_3	s'_0	s'_1	s'_2	s'_3	$r_k > 0$
Case 0: (β_0)	1	0	0	0	0	0	0	0	0	0	-
Case 1: (β_1)	1	0	1.21	2.77	22.40	0	-1.12	-12.46	-267.63	0	✓
Case 2: (β_2)	1	0	4.37	-4	2.62	17.60	-1.55	-2	-6.21	-160.51	✗
Case 3: (β_3)	1	0	-1	1.94	2.07	17.58	-0.5	-0.68	-7.16	-161.44	✗

The set of parameters obtained for the first MM complies with the stability condition (C_1) and (C_2). In the last two cases, one of the poles is fixed with a negative weight. The remaining couples of weights and poles are then computed to fit β_{toy} . Therefore, the vector fitting is used to find a set of 3 weights and poles for each MM in order to have the same degree of freedom in the optimization algorithm. The main difference between the MM parameters lies in the sign of the weights. Although the negative weights are fixed in this study in order to emphasize the consequences of not meeting the stability condition given in Section 4, the vector fitting, among others, applied on physical problems can give negative weights because of the data to fit (e.g. experimental measurements) or an ill-posed problem.

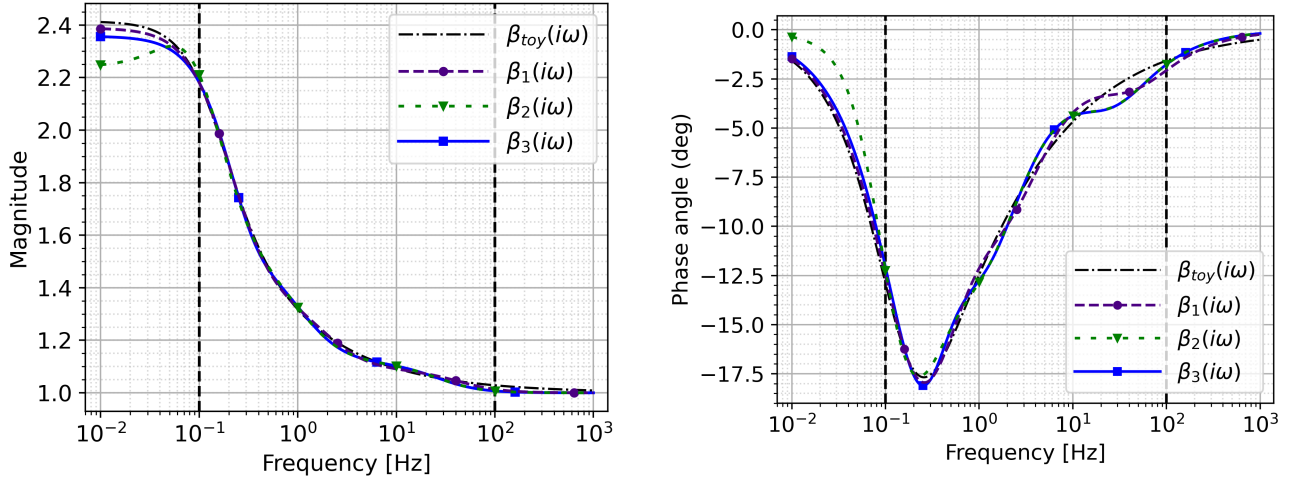


Figure 1: Bode diagram comparing β_{toy} with the MMs defined in Table 2 and obtained via the vector fitting algorithm applied on the frequency range delimited by the vertical black dashed lines.

Additionally, a comparison of the MM approximations and toy model are shown in the time domain. The focus is specifically on the function

$$\widehat{B}_{\text{toy}}(s) := \beta_{\text{toy}}(s) - 1 = \frac{\sqrt{s+2}}{s+1} = \frac{1}{s+1} + \frac{1}{\sqrt{s+2}+1}, \quad (66)$$

in order to just keep the diffusive part that is approximated. Then, the time-domain representation of (66) is

$$B_{\text{toy}}(t) = e^{-t} + \frac{e^{-2t}}{t^{0.5}} E_{0.5,0.5}(-\sqrt{t}) \quad (67)$$

where $E_{0.5,0.5}$ is the Mittag-Leffler function with two parameters (both equal to 0.5 in (67)). The latter is computed using the Mittag-Leffler function [28]. The MMs $\widehat{B}_k(s) = \beta_k(s) - 1$ are displayed in the time domain with the analytical solution (67) in Fig. 2

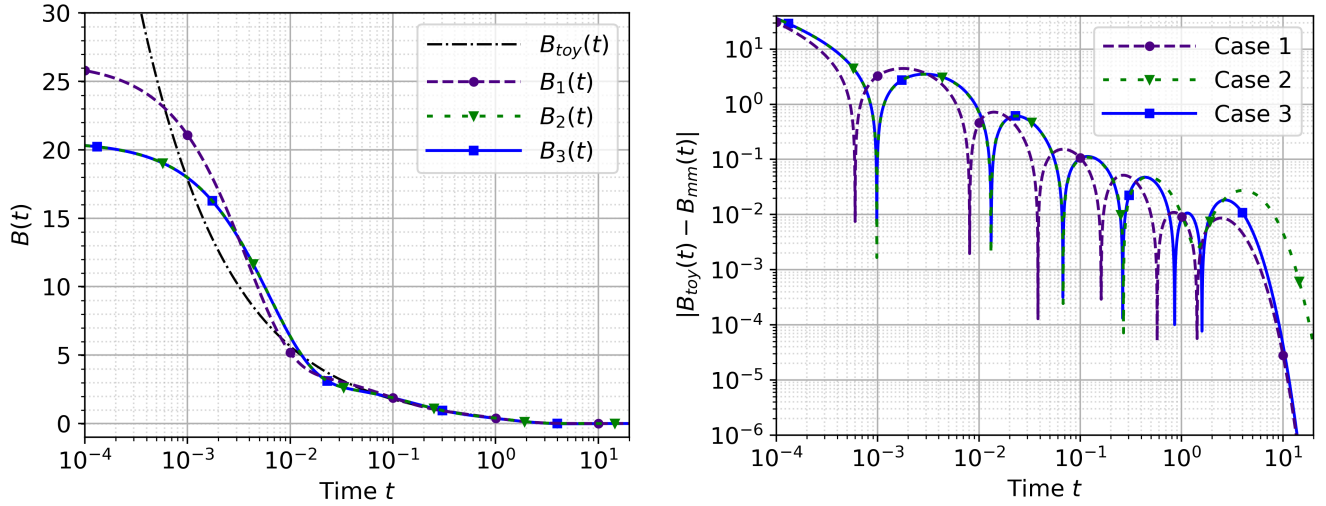


Figure 2: Time response of the MMs approximating B_{toy} (left) with the absolute error (right) when compared to the analytical solution B_{toy} .

The increasing error at short time is due to the error made at high frequencies, slightly visible on the MMs in Fig. 1. A way to improve drastically the approximation is to add parameters in the MMs. In this study, a small number of poles is deliberately chosen to highlight the impact of negative poles in a MM.

5.2.2 Numerical simulation

A square domain $\Omega = [0, 1] \times [0, 1]$ is considered and discretized with triangle elements on which polynomials of degree 5 are defined for the DG method. A non-physical porous media is assumed for the whole domain, with $\rho_0 = 1$, $\chi_0 = 1$ and $a_0 = 1$ the speed of sound in the medium without dissipation. The boundaries are taken as hard walls, and there is therefore no contribution with the exterior of Ω . The initial condition is based on a Gaussian-type source

$$p_0(x, y) = A(x - x_0) e^{-B((x-x_0)^2 + (y-y_0)^2)}, \quad (68)$$

defined in the center of Ω , i.e. $x_0 = y_0 = 0.5$. The initial velocity and pressure are

$$p(0, \mathbf{x}) = p_0(x, y), \quad (69)$$

$$\mathbf{u}(0, \mathbf{x}) = -\nabla p_0(x, y), \quad (70)$$

with $A=20$ and $B=80$. Applying the fast Fourier transform (FFT) on the initial wave, which propagates at the speed a_0 in the medium without dissipative behaviour, shows that the frequency content of the initial condition is included in $[0.1\text{Hz}, 10\text{Hz}]$. Hence, in order to have approximately 10 DG nodes for the minimal wavelength $\lambda_{\min} = a_p / f_{\max} = 0.07$ ($a_p = 1 / \sqrt{\rho_0 \chi_0 \alpha \beta}$ is the speed in the dissipative medium), the mesh is built with a space discretization $h \approx 0.08$.

The square domain with the gaussian-type source in its center is showed in Fig. 3a. For each case, the wave propagating within the rigid wall box is simulated for a given amount of time, taken dimensionless in this section. The pressure fields for cases 0 and 3 at $t = 3$ are shown in Fig. 3. The other two cases are not shown because the pressure fields are very similar to the one in Fig. 3c for $t = 3$.

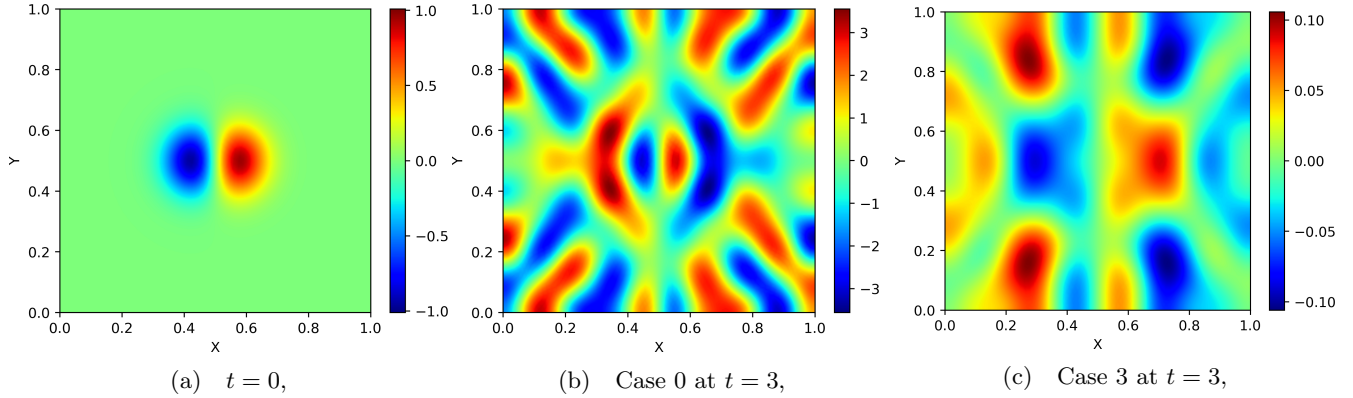


Figure 3: Pressure field at the initial time and at time $t=3$ for the non-dissipative Case 0 and the Case 3 (see Table 2). Note the change of level scales between the figures.

At each time step, the total energy in the domain is computed from equation (52). For each set of parameters, the energy normalized by its value at $t = 0$ is displayed in Fig. 4. In case 0, where no dissipation is expected, the energy is indeed constant and equal to 1 due to the normalization. In case 1, the MM only has positive weights, complying with the condition (C_2) for a stable scheme. The energy associated with this case is always decreasing, which illustrates the stability of the multipole-based EFM. Despite the trend of a decreasing energy for case 3 where negative weights are considered, the medium is *active* and creates energy at certain times, which is inconsistent with the dissipative acoustic behaviour of porous media. This unintended increasing energy phenomena is highlighted by this example, comforting the idea that, in general, working with negative weights precludes any proof of stability. However, the multipole-based EFM solved with MMs containing negative weights does not always lead to an increase of the energy, as shown with case 2, since this abnormal phenomenon may be hidden by the dissipation from the terms with positive weights. Consequently, care must be taken when working with negative weights for exclusively-dissipative acoustic porous media, and it is recommended to use only positive weights.

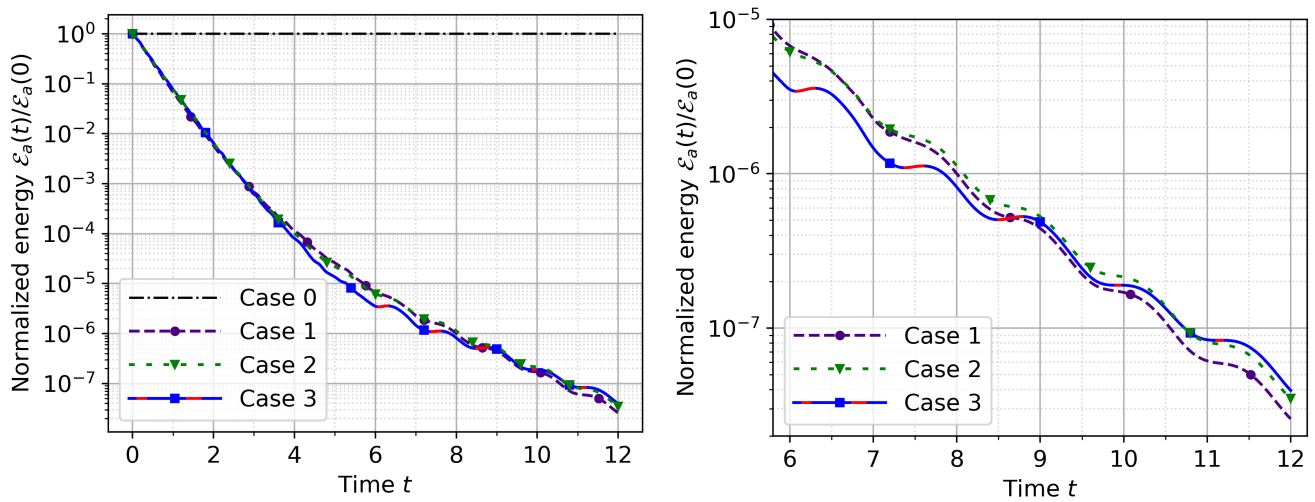


Figure 4: Energy over time for the MMs given in Tab. 2, with increasing parts of the energy marked in red. A zoom on the energy variations for $t \in [6, 12]$ is shown in the right figure.

5.3 Impedance tube simulation

In order to simulate an impedance tube experiment, the intrinsic properties of a porous sample are first used to infer the values of the chosen MM parameters. Two domains are then considered in the simulation, representing the air in the tube and the *rigidly backed* porous sample. A pulse is used as the incident wave. The numerical pressures along the tube are used to obtain the surface impedance and reflection coefficient of the sample in the frequency domain, thus mimicking an experiment.

5.3.1 Multipole-model parameters

The porous sample considered in this analysis is a melamine foam whose parameters are described in Table 2 Section 4.3 of [3], where the authors assumed that the sample is a rigid-frame porous media, and approximated its acoustic behaviour through the JCAL model. Hence, the parameters α_0 and α'_0 , which are known to be difficult to measure and to identify precisely [61], are not given. We therefore define the parameters M , N , L , M' , N' and L' in Table 3 through the JCAL model (see Table 1).

Table 3: Values of the parameters defining α and β equations (7) and (12) based on Table 2 Section 4.3 of [3].

α			β		
M	N	L	M'	N'	L'
3636.73	3636.73	3802.89	5275.18	5275.18	8355.88

Given these parameters, one is able to obtain the expressions of α and β in the whole frequency range of interest with (7) and (12). From these expressions in the frequency domain, one can attempt to retrieve the MM parameters. In this study, it is achieved using a vector fitting approach to best *fit* the transfer functions α and β on [10Hz, 10000Hz], with details about the algorithm parameters used to obtain the MMs in C.1. These fits, as well as the selected parameters, are given in Figs. 5 and 6 and Table 4, respectively. Despite the limited number of poles, an excellent agreement is obtained over the chosen frequency band, and also at the lowest frequencies. The reader is referred to C.2 for results about the convergence of the MM as a function of the number of poles for the studied case.

Table 4: Parameters of the MMs approximating α and β (Table 3) with the values in **bold** obtained analytically and the others obtained with the vector fitting (rounded to two decimals).

	c_0	c_{-1}	r_0	r_1	r_2	s_0	s_1	s_2
α_{mm}	1	3636.73	1 095.24	4 366.96	35 109.67	-6 801.60	-25 854.33	-237 436.69
β_{mm}	1	0	1 089.18	1 041.04	11 700.15	-3 866.60	-18 711.08	-179 034.54
$\tilde{\beta}_{\text{mm}}$	1	0	1 135.64	1 351.72	13 249.98	-3 926.70	-24 405.26	-227 291.46

Note that the isolated pole of β is computed analytically. Therefore, the weight r_0 and pole s_0 is straightforwardly deduced for β_{mm} . The vector fitting directly applied on β without taking into account the known single pole leads to $\tilde{\beta}_{\text{mm}}$. It will not be used further but it is given here to display the similarity between β_{mm} and $\tilde{\beta}_{\text{mm}}$, particularly the pole s_0 and weight r_0 given by the optimization procedure which are similar to the analytical ones.

5.3.2 Numerical simulation

An impedance tube is now considered, and approximated by a 2D representation. Unless explicitly mentioned, the dimensions are given in meters. A schematics of the mesh for the domain $\Omega = [0, 1] \times [0, 0.04]$, used by the fifth-order DG solver to discretize the equations is displayed in Fig. 7. Note the existence of two zones: the air $\Omega_a = [0, 0.92] \times [0, 0.04]$ associated with the blue mesh, in which the classical linearized Euler equations are solved, and the porous sample $\Omega_p = [0.92, 1] \times [0, 0.04]$ of thickness denoted $l_p = 8\text{cm}$, associated with the brown mesh, where equations (49) are solved. The porous domain is backed by a rigid wall, simulated by a fully reflective boundary condition, as for the boundary at $y = 0$ and $y = 0.04$. A non-reflecting boundary condition is imposed at the left boundary $x = 0$. At the interface between the domains, a numerical flux vector splitting is selected to weakly enforce the continuity conditions:

$$\phi_{\text{air}} u_{\text{air}} = \phi_{\text{por}} u_{\text{por}} , \quad (71)$$

$$p_{\text{air}} = p_{\text{por}} , \quad (72)$$

with $\phi_{\text{air}} = 1$.

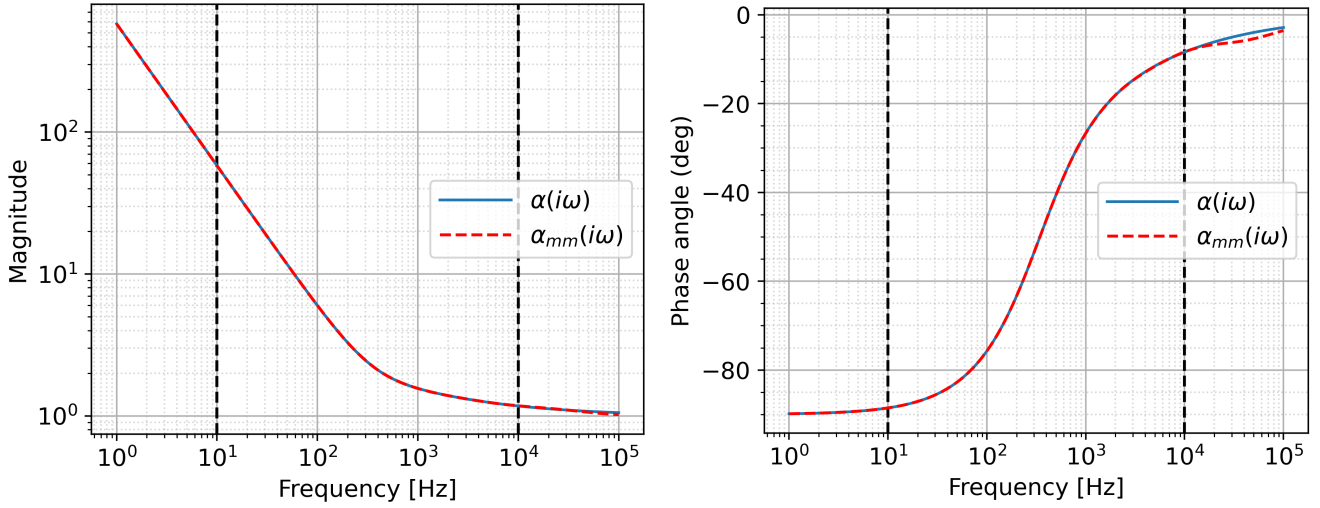


Figure 5: Bode diagram of the dynamic tortuosity α and its multipole-based approximation α_{mm} with vertical black dashed lines delimiting the frequency range of MM approximation.

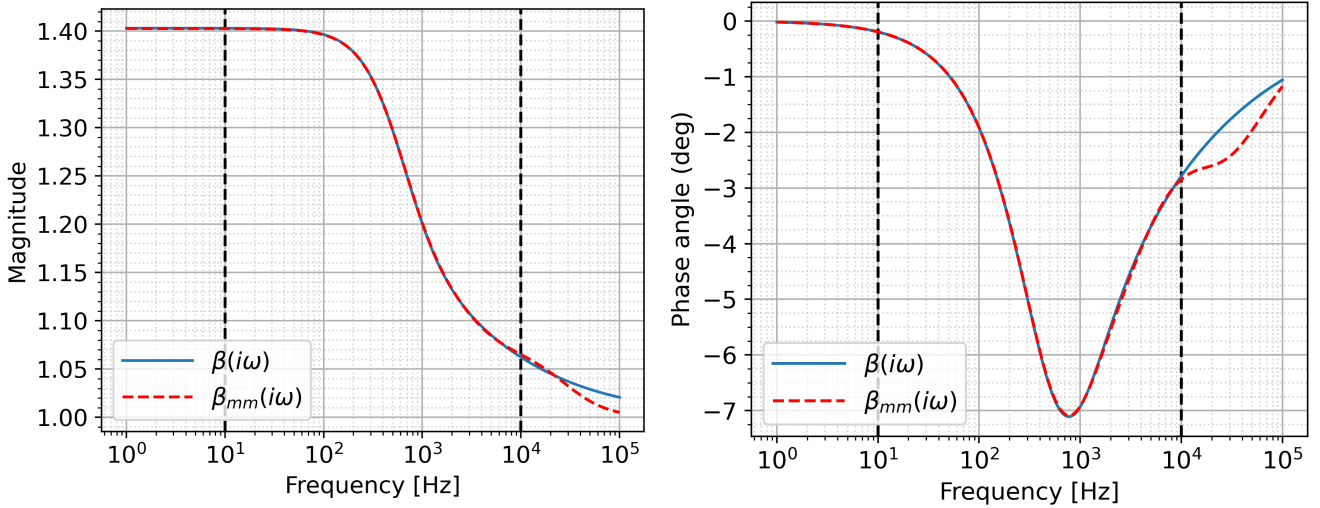


Figure 6: Bode diagram of the dynamic tortuosity β and its multipole-based approximation β_{mm} with vertical black dashed lines delimiting the frequency range of MM approximation.

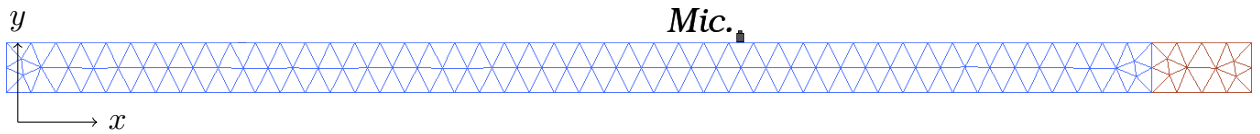


Figure 7: Mesh of the impedance tube with the microphone representing the position ($x_1 = 0.6$) where the numerical pressure is recorded.

A plane wave propagating in the tube is created by a pulse (68) initialized in the left part of the air domain:

$$p(0, \mathbf{x}) = p_0(x, 0) \quad (x < 0.2), \quad (73)$$

$$\mathbf{u}(0, \mathbf{x}) = p_0(x, 0)/(\rho_0 a_0) \quad (x < 0.2), \quad (74)$$

and null for $x > 0.2$. The values of the parameters are defined such that the frequency content extends from 100Hz to 10kHz: $x_s = 0.1$, $y_s = 0$, $A=104.28$ and $B=2000$. The mesh (and the DG order) is adapted ($h \approx 2\text{cm}$) so

that more than 10 points per wavelength are obtained at 10kHz ($\lambda_{\min} = a_p/f_{\max} = 0.5\text{cm}$). Note that in the porous sample, the speed of sound is lower than in the ambient open air ($a_p = 1/\sqrt{\rho_0 \chi_0 \alpha \beta} > a_0 = 340\text{m.s}^{-1}$). Moreover, the initialization of the simulation with a plane wave in the left part of the domain instead of a point source precludes the propagation of additional cut-on acoustic modes. Based on the highest pole in the MMs and the advection velocity constraining the stability condition (64), a time step $\Delta t = 10^{-7}\text{s}$ was selected.

The pressure is recorded at all time steps of the simulations, at one location along the side wall of the tube, to mimic a flush-mounted microphone. The microphone is located at a distance 32cm from the sample, to allow for an easy *separation* between incident and reflected waves in the time domain. Two cases are then simulated: the 1m-long tube with the porous media and a 92cm-long tube without the porous media. The recorded signals at the second location are shown in Fig. 8, where the incident wave is first seen, followed by the reflected waves (at the first interface, and then the successive waves that have travelled within the sample). An FFT analysis is then performed to analyze the signal in the frequency domain by focusing only on the reflected waves. The time zone to watch was obtained by knowing that the initial pulse is defined for $x \in [0, 0.2]$ and it travels in the tube at 340m.s^{-1} . Consequently, the microphone will have seen all the incident wave at $t = 1.8\text{ms}$.

The transfer function of the microphone for both cases is then used to evaluate the reflection coefficient of the sample. Indeed, the pressure field inside the tube can write, in the frequency domain, as

$$P(\omega, x) = A^+ e^{-ikx} + A^- e^{+ikx}, \quad (75)$$

where $k = \omega/a_0$ is the wavenumber and A^+ and A^- the incident and reflected wave amplitudes, respectively. Moreover, the wave amplitudes are related by the reflection coefficient R through the relation $A^- = RA^+$. In the case of a rigid wall, $R = 1$. Hence, after applying the FFT on the numerical pressure of the reflected wave in both cases (with and without the porous sample), R is evaluated by dividing the frequency-dependent pressure obtained with the porous material by the frequency-dependent pressure obtained with the rigid wall.

The reflection coefficient is then used to determine the surface impedance:

$$Z(\omega) = \frac{1 + R(\omega)}{1 - R(\omega)}, \quad (76)$$

which is compared with the theoretical value:

$$Z(\omega) = -i \sqrt{\frac{\alpha(i\omega)}{\beta(i\omega)}} \cot\left(\frac{l_p}{a_0} \omega \sqrt{\alpha(i\omega) \beta(i\omega)}\right), \quad (77)$$

known for plane wave propagating in a tube containing a porous material backed by a rigid surface [2, Chap. 2]. Equation (77) is also used to display in Fig. 9 the JCAL analytical reflection coefficient, where it is compared with the reflection coefficient computed using the numerical pressure signals.

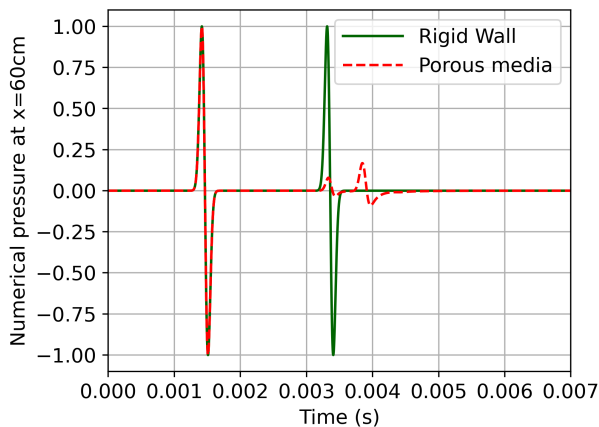


Figure 8: Numerical pressure signal over time at $(x,y) = (0.6,0.04)$, position of Mic. 2 in Fig. 7.

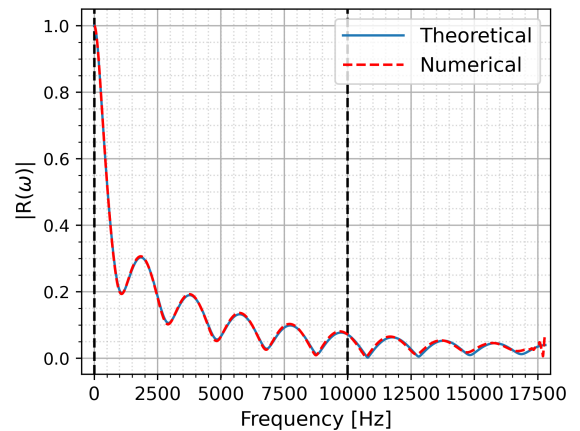


Figure 9: Absolute value of the reflection coefficient obtained with the JCAL model and computed from the numerical pressure signal. Vertical black dashed lines delimit the frequency range of MM approximation.

A comparison between the numerically evaluated impedance obtained with (76) by the numerical pressure and the initial *true* impedance computed thanks to (77) based on the JCAL model is displayed in Fig. 10. The

superimposition of the two curves in the frequency-band of interest is striking, which contributes to verify the good implementation of the method presented in Section 4. To supplement these results, a detailed analysis on the level of error between the theoretical and numerical results is given in D.

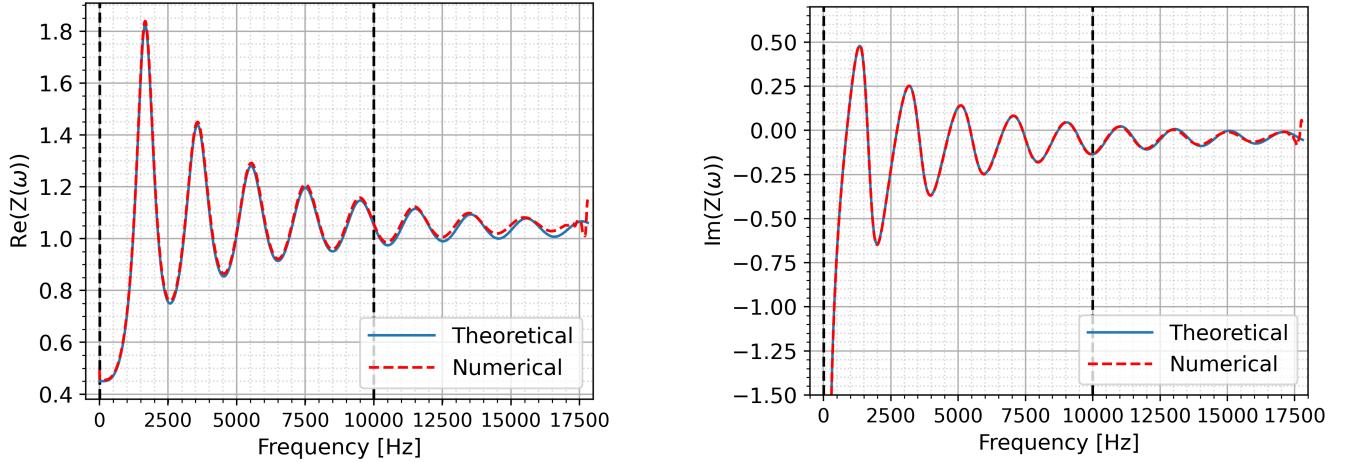


Figure 10: Real (left) and imaginary (right) part of the surface impedance with vertical black dashed line delimiting the frequency range of MM approximation.

The present approach represents rigid porous media in a volumic way, as opposed to a time-domain impedance boundary condition (TDIBC) [52] where liners are considered as a surface boundary condition. The latter approach also relies on the oscillo-diffusive representation of a time-domain operator. While useful for classical acoustic liners based on a single degree of freedom (perforated plate over cavity), the TDIBC approach could show its limits for complex materials (i.e., meta-surface and multi-layer liners), as the impedance operator could become too complex for the diffusive representation to handle. On the other hand, the present approach can represent individually each element of such a complex acoustic liner at the price of an extended simulation domain. The operators that need to be discretized remain α and β , and do not gain in complexity, since they are associated with individual materials.

Moreover, the results of this section show that with only 3 poles in the MMs for each dynamic variables, α and β , a fine approximation of the porous-media acoustic behaviour can be done over 3 frequency decades. They are also quite correct outside the frequency range of approximation for almost twice the maximum frequency of the range of approximation. Additional tests (not shown here for conciseness) showed that, in general, MMs fitting the JCAPL model for a narrow band of frequencies gives a well-approximated model over a wider range of frequencies. This behaviour could be explained by the smoothness of the JCAPL model. Hence, for instance, ultrasound waves, where a significant amount of anti-resonances are present per decade, could be well approximated with a small amount of poles.

6 Conclusion

A formulation of the JCAPL model for wave propagation in rigid isotropic media was proposed in the time domain. Both the dynamic tortuosity α and compressibility β were defined with an oscillatory-diffusive (OD) representation with positive weights. The initial set of equations was then recast into an augmented system in the time domain, where diffusive variables are used as a time-local representation of the convolution operators. Expressing the JCAPL-EFM with an OD representation allowed the proof of its stability. This representation provides insights into the behaviour of the model and helps guiding the choices made when approximating the model. A similar approach can also cover the stability proof of the Horoshenkov-EFM, which shows the possible use of our method for other models than those treated in the present work.

In addition to the JCAPL and Horoshenkov models, the Wilson model was shown to admit a diffusive representation. These representations consist of a continuous superposition of first-order systems which are straightforwardly discretized as a multipole model (MM) with a finite number of first-order systems whose poles are real-valued. It is consistent with the existing time-domain studies in the literature [13, 69] on porous materials without locally-resonant behaviour [3], for which MMs with real parameters are used. The same approach can also be applied

to metamaterials with known expressions of the dynamic variables, with the distinction that complex conjugate parameters may arise. Hence, MMs appear to be a well-suited approximation for several models of α and β .

From this observation and the diffusive-based JCAPL-EFM, a multipole-based approximation was adopted to approach the model prior to its numerical implementation in an acoustic 2D DG solver. A stability analysis was performed on the multipole-based version of the EFM. A sufficient stability condition was found to be the positivity of all the weights in the MM terms, a condition similar to the positivity of the diffusive weight needed to prove the stability of the JCAPL-EFM.

A numerical analysis was conducted to illustrate the stability condition on a toy model, highlighting possible non-dissipative phenomena for MM having negative weights. A more involved numerical simulation was then performed in a multi-zone domain, to validate the numerical integration with analytical data mimicking an impedance tube experiment.

A perspective for future studies consists in relaxing the rigid-frame hypothesis, in order to work with poroelastic materials. Another avenue of research could be the extension of the present work to inhomogeneous materials. Both these considerations could benefit the fields of acoustics, biomechanics and geophysics.

Acknowledgment This research has been financially supported by ONERA and by ISAE-SUPAERO, through the EUR TSAE under grant ANR-17-EURE-0005.

A Representation of the dynamic variables

This appendix recalls the expression of the JCAPL, Wilson and Horoshenkov models and gathers their reformulation based on an OD representation.

A.1 Johnson-Champoux-Allard-Pride-Lafarge model

The JCAPL model is recalled below with the parameters M, N, L, M', N' and L' defined in Section 2.

$$\alpha(s) = \alpha_\infty \left[1 + \frac{M}{s} + N \frac{\sqrt{1 + \frac{s}{L}} - 1}{s} \right] \quad (s \in \mathbb{C} \setminus (-\infty, -L]), \quad (78)$$

$$\beta(s) = \gamma - (\gamma - 1) \left[1 + \frac{M'}{s} + N' \frac{\sqrt{1 + \frac{s}{L'}} - 1}{s} \right]^{-1} \quad (s \in \mathbb{C} \setminus (-\infty, -L']). \quad (79)$$

The peculiarity of (79) lies in the oscillatory part of its OD representation (19) which exists under the condition (17) given in Section 2. The steps to obtain this condition are detailed below, followed by the expressions of the isolated pole and its associated weight when they exist.

The function studied is first recalled:

$$\beta_{\text{od}}(s) := \frac{\beta(s) - 1}{\gamma - 1} = \frac{M' + N' \left(\sqrt{1 + \frac{s}{L'}} - 1 \right)}{s + N' \sqrt{1 + \frac{s}{L'}} + M' - N'} \quad (s \in \mathbb{C} \setminus (-\infty, -L']). \quad (80)$$

The diffusive part of (80) is computed with (54). However, just by looking at the expression of β_{od} , one can speculate on the existence of singularities which are directly linked to the oscillatory part. Therefore, the focus is on the denominator of (80), and specifically on its zeros. Let us then define:

$$Q(s) := s + N' \sqrt{1 + \frac{s}{L'}} + M' - N' \quad (s \in \mathbb{C} \setminus (-\infty, -L']). \quad (81)$$

A change of variables $\varphi : \lambda \rightarrow L'(\lambda^2 - 1)$ simplifies the expression (81) into a second-order polynomial:

$$\tilde{Q}(\lambda) := Q(\varphi(\lambda)) = L'\lambda^2 + N'\lambda + (M' - N' - L') \quad (\Re(\lambda) > 0). \quad (82)$$

As a result, any root λ_r of \tilde{Q} with a positive real part implies that β_{od} has a singularity at $\varphi^{-1}(\lambda_r)$. A brief study of the imaginary part of (82) shows that \tilde{Q} does not admit any root in $\mathbb{C}_0^+ \setminus \mathbb{R}^+$, with $\mathbb{C}_0^+ = \{s \in \mathbb{C} \mid \Re(s) > 0\}$. Hence, the roots of \tilde{Q} on \mathbb{C}^+ are necessarily real, if they exist. Then, by solving the polynomial on \mathbb{R} , we find that:

- if $M' - N' - L' > 0$, then $\tilde{Q}(\lambda) > 0$ for all positive real λ (however, \tilde{Q} may have negative roots),
- if $M' - N' - L' < 0$, then there exists two roots of \tilde{Q} . If it is the case, one of the roots is always negative and the other, denoted λ_0 , is always included in $]0, 1[$.

In the second case where $M' - N' - L'$ is negative, the positive root of \tilde{Q} can be shown to be in $]0, 1[$ by simply noticing that $\tilde{Q}(0) = M' - N' - L' < 0$ and $\tilde{Q}(1) = M' > 0$. These results are highlighted Fig. 11 with both cases displayed.

In that respect, one can conclude that in the second case, i.e. $M' - N' - L' < 0$, β_{od} has a singularity at s_0 parametrized by λ_0 , which leads to the existence of an oscillatory part. Moreover, the weight r_0 associated with the pole s_0 is the residue of β_{od} at s_0 , defined as:

$$r_0 := \lim_{\epsilon \rightarrow 0} \frac{1}{2j\pi} \oint_{|s-s_0|=\epsilon} \beta_{\text{od}}(s) ds.$$

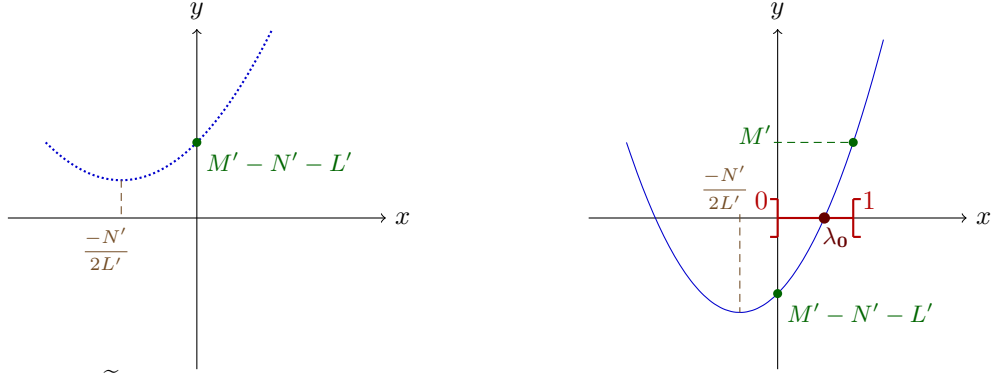


Figure 11: Polynomial \tilde{Q} for two set of parameters: the dotted line (.....) is associated with the case $\mathbf{M}' - \mathbf{N}' - \mathbf{L}' > \mathbf{0}$, the solid line (—) is associated with the case $\mathbf{M}' - \mathbf{N}' - \mathbf{L}' < \mathbf{0}$.

Consequently, under condition (17) for the existence of an isolated pole, β_{od} consists of a single pole and a diffusive part, both obtained by using the Bromwich contour Fig. 12:

$$\beta_{\text{od}}(s) = \frac{r_0}{s - s_0} + N' \int_{L'}^{\infty} \frac{\nu(\xi)}{s + \xi} d\xi \quad (\Re(s) > 0), \quad (83)$$

$$\text{where } \nu(\xi) := \frac{1}{\pi} \frac{\xi \sqrt{\frac{\xi}{L'} - 1}}{(\xi - M' + N')^2 + N'^2 \left(\frac{\xi}{L'} - 1\right)} \quad (\xi \in]L', +\infty[), \quad (84)$$

$$s_0 := L' (\lambda_0^2 - 1) < 0, \quad (85)$$

$$r_0 := 2L' \lambda_0 \frac{M' + N'(\lambda_0 - 1)}{2L' \lambda_0 + N'} > 0, \quad (86)$$

$$\text{with } \lambda_0 := \frac{-N' + \sqrt{N'^2 - 4L'(M' - N' - L')}}{2L'}, \quad (87)$$

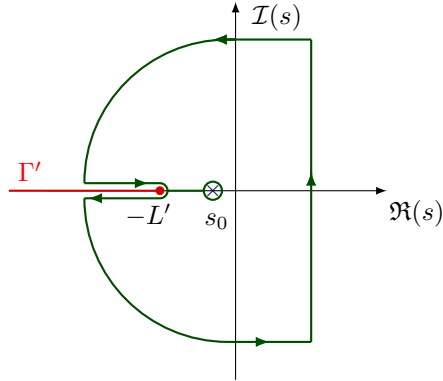


Figure 12: Bromwich contour used to find the OD representation of the dynamic compressibility β .

Therefore, the normalized dynamic compressibility is expressed as follows:

$$\beta(s) = 1 + (\gamma - 1) \left[\frac{r_0}{s - s_0} + N' \int_{L'}^{\infty} \frac{\nu(\xi)}{s + \xi} d\xi \right] \quad (\Re(s) > 0). \quad (88)$$

Based on the values taken by λ_0 , the residue r_0 is always positive while the pole s_0 is always negative if it exists.

A.2 Wilson model

The Wilson model describes the dynamic tortuosity and the normalized dynamic compressibility as follows:

$$\alpha_w(s) = \frac{(1 + \tau_v s)^{1/2}}{(1 + \tau_v s)^{1/2} - 1} \quad (s \in \mathbb{C} \setminus (-\infty, -\tau_v^{-1}]), \quad (89)$$

$$\beta_w(s) = \frac{(1 + \tau_e s)^{1/2}}{(1 + \tau_e s)^{1/2} + \gamma - 1} \quad (s \in \mathbb{C} \setminus (-\infty, -\tau_e^{-1}]), \quad (90)$$

where τ_v and τ_e are the vorticity-mode relaxation time and the entropy-mode relaxation time, respectively. A simple diffusive representation (20) is proposed for (90) in Section 2 and recalled below with the expression of the associated negative diffusive weight.

$$\beta_w(s) = 1 + (\gamma - 1) \int_{\tau_e^{-1}}^{\infty} \frac{\nu_w(\xi)}{s + \xi} d\xi \quad (\Re(s) > 0), \quad (91)$$

$$\text{with } \nu_w(\xi) = \frac{-1}{\pi} \frac{\sqrt{\tau_e \xi - 1}}{(\tau_e \xi - 1) + (\gamma - 1)^2} \quad (\xi \in [\tau_e^{-1}, +\infty)). \quad (92)$$

Here, we look for another representation of β_w with a positive diffusive weight. For this purpose, we worked on the following function:

$$\frac{\beta_w(s)}{1 + \tau_e s} = \frac{1}{(1 + \tau_e s) + (\gamma - 1)(1 + \tau_e s)^{1/2}} \quad (s \in \mathbb{C} \setminus (-\infty, -\tau_e^{-1}]), \quad (93)$$

which admits a diffusive representation:

$$\frac{\beta_w(s)}{1 + \tau_e s} = \int_{\tau_e^{-1}}^{\infty} \frac{\tilde{\nu}_w(\xi)}{s + \xi} d\xi \quad (\Re(s) > 0), \quad (94)$$

$$\text{with } \tilde{\nu}_w(\xi) = \frac{1}{\pi} \frac{\sqrt{\tau_e \xi - 1}}{(\tau_e \xi - 1)^2 + (\gamma - 1)^2 (\tau_e \xi - 1)} \quad (\xi \in (\tau_e^{-1}, +\infty)). \quad (95)$$

It leads to express β_w as a sum of a diffusive representation and an extended diffusive representation:

$$\beta_w(s) = (\gamma - 1) \int_{\tau_e^{-1}}^{\infty} \frac{\tilde{\nu}_w(\xi)}{s + \xi} d\xi + (\gamma - 1) \tau_e \int_{\tau_e^{-1}}^{\infty} \tilde{\nu}_w(\xi) \frac{s}{s + \xi} d\xi \quad (\Re(s) > 0), \quad (96)$$

The first term of the right-hand side of (96) is a conventional diffusive part, and the last term of the right-hand side is said to be extended by differentiation because of the factor s .

A.3 Horoshenkov model

The dynamic variables expressed by the Horoshenkov model are described in the Laplace domain:

$$\alpha_h(s) = \alpha_\infty \left[1 + \frac{M_h}{s} + N_h \frac{1}{\sqrt{\frac{s}{L_h} + 1}} \right] \quad (s \in \mathbb{C} \setminus (-\infty, -L]), \quad (97)$$

$$\beta_h(s) = \gamma - (\gamma - 1) \left[1 + \frac{M'_h}{s} + N'_h \frac{1}{\sqrt{\frac{s}{L'_h} + 1}} \right]^{-1} \quad (s \in \mathbb{C} \setminus (-\infty, -L']), \quad (98)$$

where $M_h = \nu\phi/(k_0\alpha_\infty)$, $N_h = \theta_{\rho,1}$ and $L_h = M_h/\theta_{\rho,3}^2$ for the dynamic tortuosity and $M'_h = \nu\phi/(k'_0\text{Pr})$, $N'_h = \theta_{c,1}$ and $L'_h = M'_h/\theta_{c,3}^2$ for the normalized dynamic compressibility. $\theta_{\rho,1}$, $\theta_{\rho,3}$, $\theta_{c,1}$ and $\theta_{c,3}$ are the Padé approximant parameters used in the Horoshenkov model [35, 36]. A comparison between the Horoshenkov model (97)-(98) and the JCPL model (78)-(79) highlights similarities between their expressions and one different term which implies different OD representations.

The normalized dynamic compressibility of the Horoshenkov model admits a diffusive representation:

$$\beta_h(s) = 1 + (\gamma - 1) N'_h \int_0^\infty \frac{\nu_h(\xi)}{s + \xi} d\xi \quad (\Re(s) > 0), \quad (99)$$

$$\text{with } \nu_h(\xi) = \frac{1}{\pi} \frac{\xi^2 \sqrt{\frac{\xi}{L'_h}}}{\frac{\xi}{L'_h} (\xi - M'_h)^2 + ((1 + N'_h)\xi - M'_h)^2} > 0 \quad (\xi \in [0, +\infty)). \quad (100)$$

B Multipole-based model

This section details system (49), written in hyperbolic form (54), and the analogous system obtained without applying the partial fraction decomposition (47). First, system (49) is detailed below:

$$\begin{aligned} \partial_t \begin{pmatrix} u \\ v \\ p \\ \Phi^X \\ \Phi^Y \\ \Psi \end{pmatrix} + \begin{pmatrix} 0 & 0 & \frac{1}{\rho_0 c_0} & O^r & O^r & O^r \\ 0 & 0 & 0 & O^r & O^r & O^r \\ \frac{1}{\chi_0 c'_0} & 0 & 0 & O^r & O^r & O^r \\ O^c & O^c & O^c & O & O & O \\ O^c & O^c & O^c & O & O & O \\ O^c & O^c & O^c & O & O & O \end{pmatrix} \partial_x \begin{pmatrix} u \\ v \\ p \\ \Phi^X \\ \Phi^Y \\ \Psi \end{pmatrix} + \begin{pmatrix} 0 & 0 & 0 & O^r & O^r & O^r \\ 0 & 0 & \frac{1}{\rho_0 c_0} & O^r & O^r & O^r \\ 0 & \frac{1}{\chi_0 c'_0} & 0 & O^r & O^r & O^r \\ O^c & O^c & O^c & O & O & O \\ O^c & O^c & O^c & O & O & O \\ O^c & O^c & O^c & O & O & O \end{pmatrix} \partial_y \begin{pmatrix} u \\ v \\ p \\ \Phi^X \\ \Phi^Y \\ \Psi \end{pmatrix} + \\ \begin{pmatrix} \frac{c-1}{c_0} + \sum_{k=1}^K \frac{r_k}{c_0} & 0 & 0 & \frac{RS}{c_0} & O^r & O^r \\ 0 & \frac{c-1}{c_0} + \sum_{k=1}^K \frac{r_k}{c_0} & 0 & O^r & \frac{RS}{c_0} & O^r \\ 0 & 0 & \frac{c'-1}{c'_0} + \sum_{k=1}^{K'} \frac{r'_k}{c'_0} & O^r & O^r & \frac{R'S'}{c'_0} \\ -\mathbf{1} & O^c & O^c & -S & O & O \\ O^c & -\mathbf{1} & O^c & O & -S & O \\ O^c & O^c & -\mathbf{1} & O & O & -S' \end{pmatrix} \begin{pmatrix} u \\ v \\ p \\ \Phi^X \\ \Phi^Y \\ \Psi \end{pmatrix} = 0, \end{aligned} \quad (101)$$

where:

- the row vectors are:

$$\begin{aligned} RS &= (r_1 s_1 \quad r_2 s_2 \quad \dots \quad r_{K-1} s_{K-1} \quad r_K s_K), \\ R'S' &= (r'_1 s'_1 \quad r'_2 s'_2 \quad \dots \quad r'_{K-1} s'_{K-1} \quad r'_K s'_K), \end{aligned}$$

- the pole matrices are:

$$S = \begin{pmatrix} s_1 & 0 & \dots & \dots & 0 \\ 0 & s_2 & \ddots & & \vdots \\ \vdots & \ddots & \ddots & \ddots & \vdots \\ \vdots & & \ddots & s_{K-1} & 0 \\ 0 & \dots & \dots & 0 & s_K \end{pmatrix}, \quad \text{and} \quad S' = \begin{pmatrix} s'_1 & 0 & \dots & \dots & 0 \\ 0 & s'_2 & \ddots & & \vdots \\ \vdots & \ddots & \ddots & \ddots & \vdots \\ \vdots & & \ddots & s'_{K-1} & 0 \\ 0 & \dots & \dots & 0 & s'_K \end{pmatrix},$$

- the all-ones column vector is: $\mathbf{1} = \begin{pmatrix} 1 \\ \vdots \\ 1 \end{pmatrix},$

- the zero matrices are: O (square matrix), O^r (row matrix) and O^c (column matrix).

Starting from the EFM equations and the multipole-based approximations (45) and (46) of α and β , respectively,

the system in the Laplace domain writes:

$$\begin{cases} s \hat{\mathbf{u}} + \frac{c_{-1}}{c_0} \hat{\mathbf{u}} + \sum_{k=1}^K \frac{r_k}{c_0} \frac{s}{s-s_k} \hat{\mathbf{u}} = -\frac{1}{\rho_0 c_0} \nabla \hat{p}, \\ s \hat{p} + \frac{c'_{-1}}{c'_0} \hat{p} + \sum_{k=1}^{K'} \frac{r'_k}{c'_0} \frac{s}{s-s'_k} \hat{p} = -\frac{1}{\chi_0 c'_0} \nabla \cdot \hat{\mathbf{u}}, \end{cases} \quad (102)$$

In contrast to (48), no partial fraction decomposition is applied in (102). Applying the inverse Laplace transform on (102) leads to the time-domain system

$$\begin{cases} \partial_t \mathbf{u} + \frac{1}{\rho_0 c_0} \nabla p + \frac{c_{-1}}{c_0} \mathbf{u} + \sum_{k=1}^K \frac{r_k}{c_0} \phi_{\mathbf{k}} = 0, \end{cases} \quad (103a)$$

$$\begin{cases} \partial_t p + \frac{1}{\chi_0 c'_0} \nabla \cdot \mathbf{u} + \frac{c'_{-1}}{c'_0} p + \sum_{k=1}^{K'} \frac{r'_k}{c'_0} \psi_k = 0, \end{cases} \quad (103b)$$

$$\begin{cases} \partial_t \phi_{\mathbf{k}} = s_k \phi_{\mathbf{k}} + \partial_t \mathbf{u} \quad (\forall k \in \llbracket 1, K \rrbracket), \end{cases} \quad (103c)$$

$$\begin{cases} \partial_t \psi_k = s'_k \psi_k + \partial_t p \quad (\forall k \in \llbracket 1, K' \rrbracket), \end{cases} \quad (103d)$$

which writes

$$\begin{cases} \partial_t \mathbf{u} + \frac{1}{\rho_0 c_0} \nabla p + \frac{c_{-1}}{c_0} \mathbf{u} + \sum_{k=1}^K \frac{r_k}{c_0} \phi_{\mathbf{k}} = 0, \end{cases} \quad (104a)$$

$$\begin{cases} \partial_t p + \frac{1}{\chi_0 c'_0} \nabla \cdot \mathbf{u} + \frac{c'_{-1}}{c'_0} p + \sum_{k=1}^{K'} \frac{r'_k}{c'_0} \psi_k = 0, \end{cases} \quad (104b)$$

$$\begin{cases} \partial_t \phi_{\mathbf{k}} + \frac{1}{\rho_0 c_0} \nabla p + \frac{c_{-1}}{c_0} \mathbf{u} + \sum_{j=1}^K \frac{r_j}{c_0} \phi_{\mathbf{j}} - s_k \phi_{\mathbf{k}} = 0 \quad (\forall k \in \llbracket 1, K \rrbracket), \end{cases} \quad (104c)$$

$$\begin{cases} \partial_t \psi_k + \frac{1}{\chi_0 c'_0} \nabla \cdot \mathbf{u} + \frac{c'_{-1}}{c'_0} p + \sum_{j=1}^{K'} \frac{r'_j}{c'_0} \psi_j - s'_k \psi_k = 0 \quad (\forall k \in \llbracket 1, K' \rrbracket). \end{cases} \quad (104d)$$

after replacing the derivatives in the auxiliary equations (103c) and (103d) by using (103a) and (103b) respectively. The hyperbolic form of (104) reads

$$\partial_t \mathbf{q} + \widetilde{A}_x \partial_x \mathbf{q} + \widetilde{A}_y \partial_y \mathbf{q} + \widetilde{B} \mathbf{q} = \mathbf{F}, \quad (105)$$

where \mathbf{q} is given in Section 5 and

$$\widetilde{A}_x = \begin{pmatrix} 0 & 0 & \frac{1}{\rho_0 c_0} & 0 & \dots & \dots & \dots & 0 \\ 0 & 0 & 0 & 0 & \dots & \dots & \dots & 0 \\ \frac{1}{\chi_0 c'_0} & 0 & 0 & 0 & \dots & \dots & \dots & 0 \\ 0 & 0 & \frac{1}{\rho_0 c_0} & 0 & \dots & \dots & \dots & 0 \\ \vdots & \vdots \\ 0 & 0 & \frac{1}{\rho_0 c_0} & 0 & \dots & \dots & \dots & 0 \\ 0 & 0 & 0 & 0 & \dots & \dots & \dots & 0 \\ \vdots & \vdots \\ \frac{1}{\chi_0 c'_0} & 0 & 0 & 0 & \dots & \dots & \dots & 0 \\ \vdots & \vdots \\ \frac{1}{\chi_0 c'_0} & 0 & 0 & 0 & \dots & \dots & \dots & 0 \end{pmatrix}, \quad \widetilde{A}_y = \begin{pmatrix} 0 & 0 & 0 & 0 & \dots & \dots & \dots & 0 \\ 0 & 0 & \frac{1}{\rho_0 c_0} & 0 & \dots & \dots & \dots & 0 \\ 0 & \frac{1}{\chi_0 c'_0} & 0 & 0 & \dots & \dots & \dots & 0 \\ 0 & 0 & 0 & 0 & \dots & \dots & \dots & 0 \\ \vdots & \vdots \\ 0 & 0 & 0 & 0 & \dots & \dots & \dots & 0 \\ 0 & 0 & \frac{1}{\rho_0 c_0} & 0 & \dots & \dots & \dots & 0 \\ \vdots & \vdots \\ 0 & 0 & \frac{1}{\rho_0 c_0} & 0 & \dots & \dots & \dots & 0 \\ 0 & \frac{1}{\chi_0 c'_0} & 0 & 0 & \dots & \dots & \dots & 0 \\ \vdots & \vdots \\ 0 & \frac{1}{\chi_0 c'_0} & 0 & 0 & \dots & \dots & \dots & 0 \end{pmatrix} \left. \begin{array}{l} \left. \begin{array}{l} (u, v, p) \\ \phi_{\mathbf{k}}^X \\ \phi_{\mathbf{k}}^Y \\ \psi_k \end{array} \right\} \right\} \end{array} \right\} \quad (106)$$

C Parameter selection and convergence of the vector fitting algorithm

This Appendix describes the way vector fitting was used in this work. Details on the convergence of the MM for the JCAPL model are also given.

C.1 Multipole-model approximation via vector fitting

In this article, the approach used to build the MMs is the *vector fitting* for which detailed results are given in [30]. The MMs built with this algorithm depends on the behaviour of the complex-valued function to approximate, the physical parameters, the frequency range of approximation and the optimization-algorithm parameters (starting poles, number of iterations, degrees of freedom). For example, in the toy model case Section 5.2, the MM approximation is being sought as:

$$\widehat{B}_{\text{MM}}(s) = \sum_k \frac{r_k}{s - s_k}. \quad (107)$$

The vector fitting can take into account an additional constant parameter, denoted c_0 herein, as a degree of freedom to improve the approximation on the delimited frequency range.

$$\widehat{B}_{\text{MM}c}(s) = \sum_k \frac{r_k}{s - s_k} + c_0. \quad (108)$$

By doing so, the approximation \widehat{B}_4 of β_{toy} , built as (108), is different from $\widehat{B}_1 = \beta_1 - 1$, built as (107) with the same amount of poles. The parameters of the two MMs are given in Table 5 describing two different time responses, and therefore, describing different errors when compared with the toy-model time response. This is shown in Fig. 13. Hence, a study on the vector fitting applied to the JCAPL model should not be straightforwardly generalized to other problems and other initialization parameters of the vector fitting.

Table 5: Parameters of the multipole toy models associated with case 1 studied in section 5.2 (Table 2) and case 4 for which the constant value c'_0 is a parameter of the *vector fitting*.

	Constant	Weights			Poles		
	c'_0	r'_0	r'_1	r'_2	s'_0	s'_1	s'_2
Case 1: (\widehat{B}_1)	0	1.21	2.77	22.40	-1.12	-12.46	-267.63
Case 4: (\widehat{B}_4)	0.03	1.15	1.89	8.20	-1.07	-8.79	-91.19

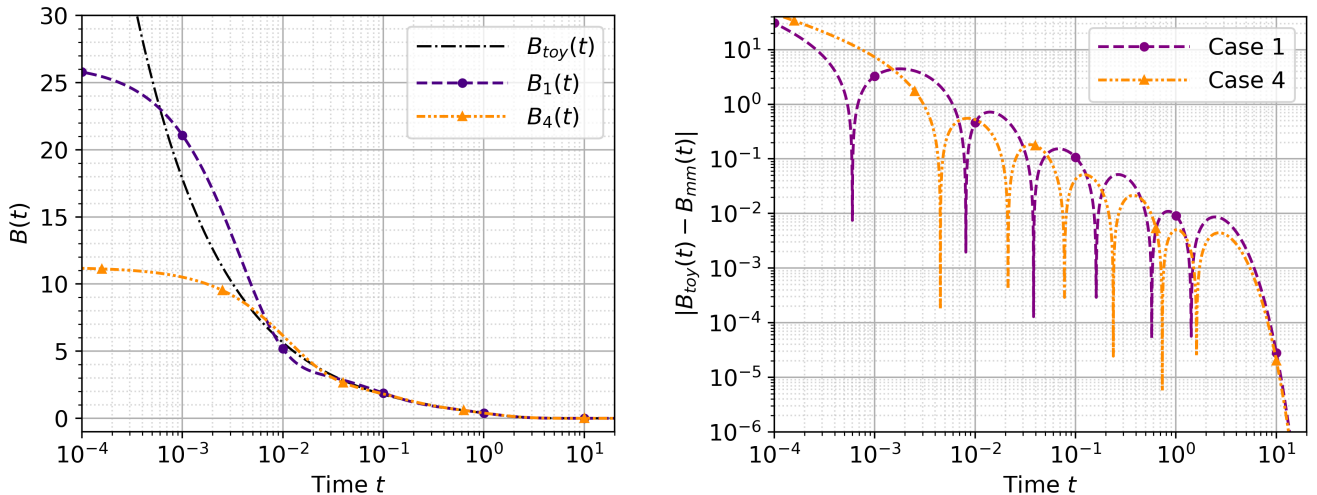


Figure 13: Time response of the MM 1 and 4 approximating B_{toy} (left) with the absolute error (right) when compared to the analytical solution B_{toy} .

The description of the algorithm parameters used for the different studies of the present article are gathered in this paragraph. First, the approximation is always done on the diffusive part of the studied transfer functions ($\beta_{\text{toy}} - 1$ for the toy model equation (65) in section 5.2.1, α_d and β_{od} given in equations (8) and (13)). This choice originates from the seek of an approximation of solely the irrational terms that complexify the time-domain problem. For instance, an MM approximation of the whole JCAPL- α expression (7) can be obtained, but leads to approximate terms as $\alpha_\infty M/s$ which inverse Laplace transform are known and straightforwardly tackled. Second, the three main points of the algorithm initialization that were varied in this study are: the starting pole values, the number of iteration of the algorithm and the number of poles. No additional parameters were added in the MM approximation. A wrong choice of the starting pole values can give an ill-conditioned problem. To prevent it, the poles were always logarithmically spaced in the studied frequency range and 20 iterations were chosen, which is large enough to converge to the same solution even with slightly different starting poles.

C.2 Convergence of the multipole-model approximation for the JCAPL model

In this section, the focus is on the convergence of the MM as a function of the number of poles for the JCAPL model, specifically the modified dynamic variables α_d and β_{od} defined in (8) and (13), respectively. The parameters M , N , L , M' , N' and L' , on which the modified dynamic variables depend on, are those given in Table 3. Consequently, the results shown below are given specifically for the MM approximation of the JCAPL model describing the studied melamine foam to give valuable insights of the problem, and the results should not be straightforwardly generalized to other problems.

The relative maximal error is displayed in Fig. 14 for different frequency range of approximation. The same approach to initialize the vector fitting for each number of poles and each frequency range is used, as detailed in the previous section C.1.

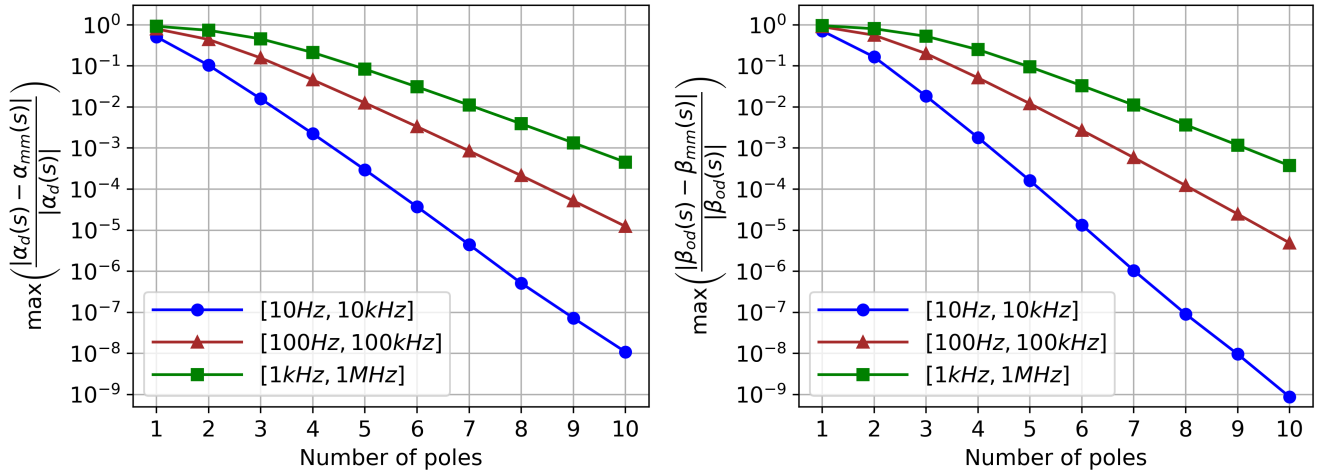
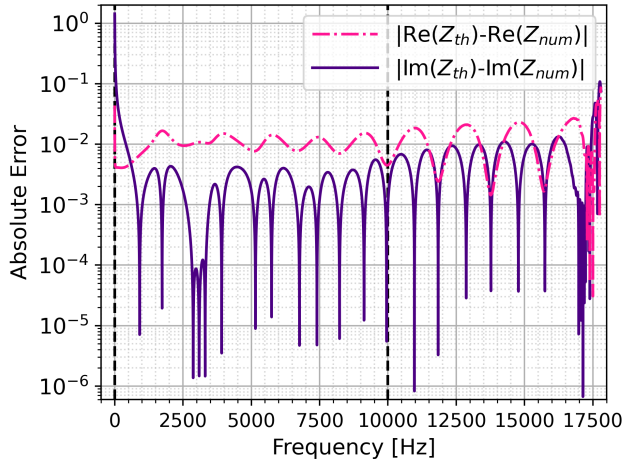


Figure 14: Relative maximal error of MMs fitting the modified dynamic variables on different frequency ranges.

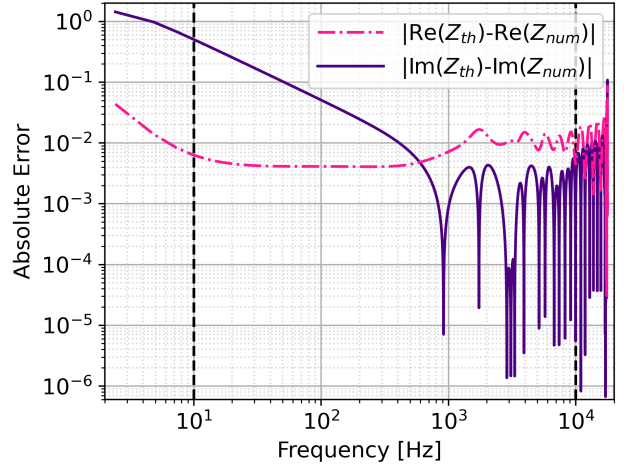
It is clear that adding poles improves the fit of MM, and Fig. 14 shows that the relative maximal error of the magnitude decreases exponentially with the number of parameters. Additionally, the larger the frequency range of interest, the higher the number of poles needed to fit a same amount of frequency decades for the JCAPL model.

D Discussion on the accuracy of the numerical impedance tube results

A closer look at the numerical results for the impedance tube simulation is given in this section. First, the absolute error on the surface impedance values is displayed in Fig. 15.



(a) Linear scale.



(b) Logarithmic scale.

Figure 15: Absolute error of the surface impedance for the impedance tube simulation with vertical black dashed lines delimiting the frequency range of MM approximation.

Figure 15b shows that the absolute error on the real part of the surface impedance is greater than for its imaginary part, except for low frequencies. However, the order of magnitude of the imaginary part varies from the real part of the surface impedance: the imaginary part is higher than the real part for low frequencies and lower for high frequencies (see Fig. 16). Furthermore, the relative errors displayed in Fig. 17 are similar for both real and imaginary parts, despite the singularities of the imaginary relative error induced by the zero values of the imaginary part. The increasing error at low frequencies is thus due to the increasing magnitude of the imaginary part at low frequencies (the relative error stays almost constant in this range of frequencies as shown in Fig. 17).

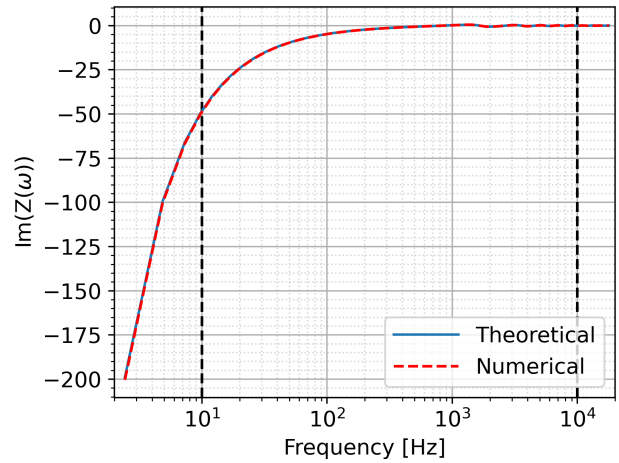
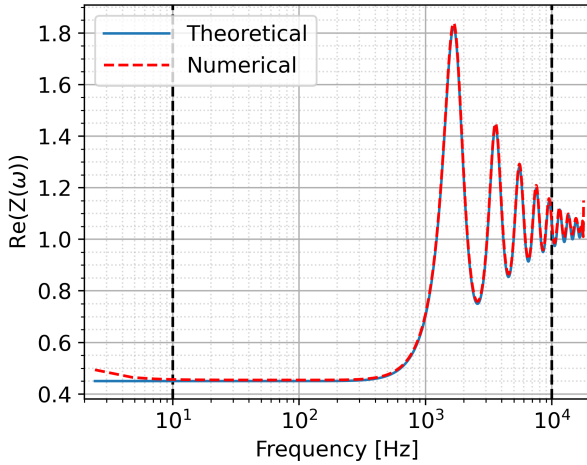


Figure 16: Real (left) and imaginary (right) part of the surface impedance with abscissa in logarithmic scale and vertical black dashed lines delimiting the frequency range of MM approximation.

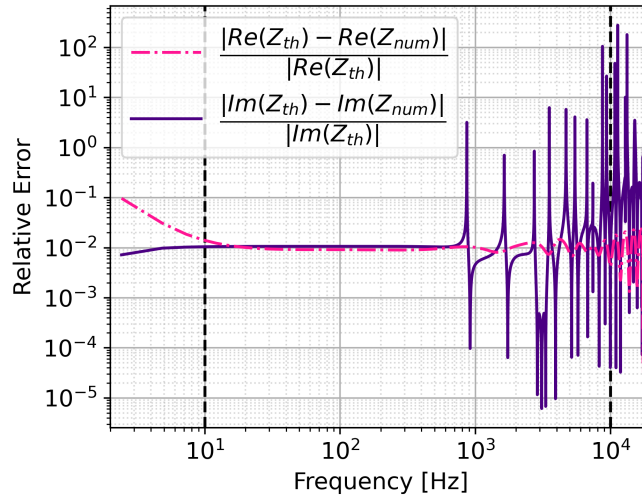


Figure 17: Relative error of the surface impedance for the impedance tube simulation with vertical black dashed lines delimiting the frequency range of MM approximation.

Consequently, the error made on the real part of the impedance is more important than on the imaginary part, but, relatively to their order of magnitude, the error is similar, estimated at 10^{-2} in the frequency range of approximation.

References

- [1] Winser Alexander and Cranos Williams. Chapter 2 - Fundamental DSP Concepts. In Winser Alexander and Cranos Williams, editors, *Digital Signal Processing*, pages 19–157. Academic Press, Boston, 2017.
- [2] Jean F. Allard and Noureddine Atalla. *Propagation of Sound in Porous Media*. John Wiley & Sons, Ltd, oct 2009.
- [3] Antoni Alomar, Didier Dragna, and Marie-Annick Galland. Pole identification method to extract the equivalent fluid characteristics of general sound-absorbing materials. *Applied Acoustics*, 174:107752, 2021.
- [4] Antoni Alomar, Didier Dragna, and Marie-Annick Galland. Time-domain simulations of sound propagation in a flow duct with extended-reacting liners. *Journal of Sound and Vibration*, 507:116137, 2021.
- [5] Jordan B. Angel, Jeffrey W. Banks, William D. Henshaw, Michael J. Jenkinson, Alexander V. Kildishev, Gregor Kovačič, Ludmila J. Prokopeva, and Donald W. Schwendeman. A high-order accurate scheme for Maxwell’s equations with a generalized dispersive material model. *Journal of Computational Physics*, 378:411–444, 2019.
- [6] Noureddine Atalla and Franck Sgard. Modeling of perforated plates and screens using rigid frame porous models. *Journal of Sound and Vibration*, 303(1):195–208, 2007.
- [7] Keith Attenborough, Imran Bashir, and Shahram Taherzadeh. Outdoor ground impedance models. *The Journal of the Acoustical Society of America*, 129(5):2806–2819, 2011.
- [8] C. Bellis and B. Lombard. Simulating transient wave phenomena in acoustic metamaterials using auxiliary fields. *Wave Motion*, 86:175 – 194, 2019.
- [9] M. A. Biot. Theory of Propagation of Elastic Waves in a Fluid-Saturated Porous Solid. I. Low-Frequency Range. *The Journal of the Acoustical Society of America*, 28(2):168–178, 1956.
- [10] M. A. Biot. Theory of Propagation of Elastic Waves in a Fluid-Saturated Porous Solid. II. Higher Frequency Range. *The Journal of the Acoustical Society of America*, 28(2):179–191, 1956.
- [11] Carolin Birk and Chongmin Song. An improved non-classical method for the solution of fractional differential equations. *Computational Mechanics*, 46(5):721–734, 2010.
- [12] Emilie Blanc, Guillaume Chiavassa, and Bruno Lombard. A time-domain numerical modeling of two-dimensional wave propagation in porous media with frequency-dependent dynamic permeability. *The Journal of the Acoustical Society of America*, 134(6):4610–4623, 2013.
- [13] Emilie Blanc, Guillaume Chiavassa, and Bruno Lombard. Biot-JKD model: Simulation of 1D transient poroelastic waves with fractional derivatives. *Journal of Computational Physics*, 237:1 – 20, 2013.
- [14] Emilie Blanc, Guillaume Chiavassa, and Bruno Lombard. Wave simulation in 2D heterogeneous transversely isotropic porous media with fractional attenuation: a Cartesian grid approach. *Journal of Computational Physics*, 275:118–142, 2014.
- [15] Leitao Cao, Qiuxia Fu, Yang Si, Bin Ding, and Jianyong Yu. Porous materials for sound absorption. *Composites Communications*, 10:25–35, 2018.
- [16] Jose M. Carcione, Dan Kosloff, and Ronnie Kosloff. Viscoacoustic wave propagation simulation in the earth. *GEOPHYSICS*, 53(6):769–777, 1988.
- [17] José Carcione, Christina Morency, and Juan Santos. Computational poroelasticity — a review. *Geophysics*, 75:75A229–75A243, 09 2010.
- [18] José M. Carcione. Wave propagation in anisotropic, saturated porous media: Plane-wave theory and numerical simulation. *The Journal of the Acoustical Society of America*, 99(5):2655–2666, 1996.
- [19] José M. Carcione. Chapter 2 - Viscoelasticity and Wave Propagation. In José M. Carcione, editor, *Wave Fields in Real Media (Third Edition)*, pages 63–122. Elsevier, Oxford, third edition edition, 2015.
- [20] Yvan Champoux and Jean-F. Allard. Dynamic tortuosity and bulk modulus in air-saturated porous media. *Journal of applied physics*, 70(4):1975–1979, 1991.

- [21] Bernardo Cockburn. Numerical resolution of Maxwell’s equations in polarisable media at radio and lower frequencies. *SIAM journal on scientific and statistical computing*, 6(4):843–852, 1985.
- [22] Gary Cohen and Sébastien Pernet. *Finite Element and Discontinuous Galerkin Methods for Transient Wave Equations*. Springer Netherlands, 2017.
- [23] Olivier Coussy. *Mechanics and physics of porous solids*. John Wiley & Sons, 2010.
- [24] Henry Philibert Gaspard Darcy. *Les Fontaines publiques de la ville de Dijon. Exposition et application des principes à suivre et des formules à employer dans les questions de distribution d’eau, etc.* V. Dalamont, 1856.
- [25] Didier Dragna, Pierre Pineau, and Philippe Blanc-Benon. A generalized recursive convolution method for time-domain propagation in porous media. *The Journal of the Acoustical Society of America*, 138(2):1030–1042, 2015.
- [26] N.F. Dudley Ward, T. Lähivaara, and S. Eveson. A discontinuous Galerkin method for poroelastic wave propagation: The two-dimensional case. *Journal of Computational Physics*, 350:690–727, 2017.
- [27] Z. E. A. Fellah, S. Berger, W. Lauriks, C. Depollier, C. Aristégui, and J.-Y. Chapelon. Measuring the porosity and the tortuosity of porous materials via reflected waves at oblique incidence. *The Journal of the Acoustical Society of America*, 113(5):2424–2433, 2003.
- [28] Roberto Garrappa. Numerical Evaluation of Two and Three Parameter Mittag-Leffler Functions. *SIAM Journal on Numerical Analysis*, 53(3):1350–1369, Jan 2015.
- [29] Robert P. Gilbert, Ying Liu, Jean-Philippe Groby, Erick Ogam, Armand Wirgin, and Yongzhi Xu. Computing porosity of cancellous bone using ultrasonic waves, II: The muscle, cortical, cancellous bone system. *Mathematical and Computer Modelling*, 50(3):421–429, 2009.
- [30] Bjorn Gustavsen and Adam Semlyen. Rational approximation of frequency domain responses by vector fitting. *IEEE Transactions on Power Delivery*, 14(3):1052–1061, 1999.
- [31] T.J. Haire and C.M. Langton. Biot theory: a review of its application to ultrasound propagation through cancellous bone. *Bone*, 24(4):291–295, 1999.
- [32] A. Hanyga and Jian-Fei Lu. Wave field simulation for heterogeneous transversely isotropic porous media with the JKD dynamic permeability. *Computational Mechanics*, 36(3):196–208, August 2005.
- [33] Thomas Hélie and Denis Matignon. Diffusive representations for the analysis and simulation of flared acoustic pipes with visco-thermal losses. *Mathematical Models and Methods in Applied Sciences*, 16(4):503–536, April 2006.
- [34] Jan S Hesthaven and Tim Warburton. *Nodal discontinuous Galerkin methods: algorithms, analysis, and applications*. Springer Science & Business Media, 2007.
- [35] Kirill V. Horoshenkov, Alistair Hurrell, and Jean-Philippe Groby. A three-parameter analytical model for the acoustical properties of porous media. *The Journal of the Acoustical Society of America*, 145(4):2512–2517, 2019.
- [36] Kirill V. Horoshenkov, Alistair Hurrell, and Jean-Philippe Groby. Erratum: A three-parameter analytical model for the acoustical properties of porous media [j. acoust. soc. am. 145(4), 2512–2517 (2019)]. *The Journal of the Acoustical Society of America*, 147(1):146–146, 2020.
- [37] Thomas Hélie and Denis Matignon. Representations with poles and cuts for the time-domain simulation of fractional systems and irrational transfer functions. *Signal Processing*, 86(10):2516 – 2528, 2006. Special Section: Fractional Calculus Applications in Signals and Systems.
- [38] David Linton Johnson, Joel Koplik, and Roger Dashen. Theory of dynamic permeability and tortuosity in fluid-saturated porous media. *Journal of fluid mechanics*, 176:379–402, 1987.
- [39] Rose M. Joseph, Susan C. Hagness, and Allen Taflov. Direct time integration of Maxwell’s equations in linear dispersive media with absorption for scattering and propagation of femtosecond electromagnetic pulses. *Opt. Lett.*, 16(18):1412–1414, Sep 1991.

- [40] J. Kergomard, D. Lafarge, and J. Gilbert. Transients in Porous Media: Exact and Modelled Time-Domain Green's Functions. *Acta Acustica united with Acustica*, 99(4):557–571, Jul 2013.
- [41] Denis Lafarge. *Propagation du son dans les matériaux poreux à structure rigide saturés par un fluide viscothermique: Définition de paramètres géométriques, analogie électromagnétique, temps de relaxation*. PhD thesis, Le Mans, 1993.
- [42] Denis Lafarge, Pavel Lemarinier, Jean F. Allard, and Viggo Tarnow. Dynamic compressibility of air in porous structures at audible frequencies. *The Journal of the Acoustical Society of America*, 102(4):1995–2006, 1997.
- [43] Bruno Lombard and Denis Matignon. Diffusive Approximation of a Time-Fractional Burger's Equation in Nonlinear Acoustics. *SIAM Journal on Applied Mathematics*, 76(5):1765–1791, 2016.
- [44] Jian-Fei Lu and Andrzej Hanyga. Wave field simulation for heterogeneous porous media with singular memory drag force. *Journal of Computational Physics*, 208(2):651–674, 2005.
- [45] Yder J. Masson and Steven R Pride. Finite-difference modeling of Biot's poroelastic equations across all frequencies. *Geophysics*, 75(2):N33 – N41, March 2010.
- [46] Denis Matignon. An introduction to fractional calculus. In Patrice Abry, Paulo Goncalves, and Jacques Levy-Vehel, editors, *Scaling, Fractals and Wavelets*, volume 1 of *Digital signal and image processing series*, pages 237–277. ISTE - Wiley, London : ISTE ; Hoboken, NJ : Wiley, 2009.
- [47] Denis Matignon and Christophe Prieur. Asymptotic stability of linear conservative systems when coupled with diffusive systems. *ESAIM: Control, Optimisation and Calculus of Variations*, 11(3):487–507, 2005.
- [48] C. Méjean, M. Badard, R. Benzerga, C. Le Paven-Thivet, and A. Sharaiha. Rigid composite materials for anechoic chamber application. *Materials Research Bulletin*, 96:94–99, 2017. The 9th international conference on the Microwave Materials and Their Applications.
- [49] Florian Monteghetti. *Analysis and Discretization of Time-Domain Impedance Boundary Conditions in Aeroacoustics*. Theses, Institut Supérieur de l'Aéronautique et de l'Espace (ISAE-SUPAERO) ; Université de Toulouse, October 2018.
- [50] Florian Monteghetti, Ghislain Haine, and Denis Matignon. Asymptotic stability of the multidimensional wave equation coupled with classes of positive-real impedance boundary conditions. *Mathematical Control & Related Fields*, 9(4):759–791, 2019.
- [51] Florian Monteghetti, Denis Matignon, and Estelle Piot. Energy analysis and discretization of nonlinear impedance boundary conditions for the time-domain linearized Euler equations. *Journal of Computational Physics*, 375:393–426, December 2018.
- [52] Florian Monteghetti, Denis Matignon, Estelle Piot, and Lucas Pascal. Design of broadband time-domain impedance boundary conditions using the oscillatory-diffusive representation of acoustical models. *The Journal of the Acoustical Society of America*, 140(3):1663–1674, 2016.
- [53] Gérard Montseny. Diffusive representation of pseudo-differential time-operators. *ESAIM: Proceedings*, 5:159–175, 1998.
- [54] Miao-Jung Yvonne Ou. On reconstruction of dynamic permeability and tortuosity from data at distinct frequencies. *Inverse Problems*, 30(9):095002, aug 2014.
- [55] Miao-Jung Yvonne Ou and Hugo J. Woerdeman. On the augmented Biot-JKD equations with Pole-Residue representation of the dynamic tortuosity. In *Interpolation and Realization Theory with Applications to Control Theory*, pages 307–328. Springer, 2019.
- [56] Florin Paun, Stéphane Gasser, and Laurent Leylekian. Design of materials for noise reduction in aircraft engines. *Aerospace science and technology*, 7(1):63–72, 2003.
- [57] Peter G. Petropoulos. The wave hierarchy for propagation in relaxing dielectrics. *Wave Motion*, 21(3):253–262, 1995.

- [58] S.R. Pride, F.D. Morgan, and A.F. Gangi. Drag forces of porous-medium acoustics. *Physical Review B*, 47(9):4964–4978, 1993. cited By 162.
- [59] R. Roncen, Z. E. A. Fellah, D. Lafarge, E. Piot, F. Simon, E. Ogam, M. Fellah, and C. Depollier. Acoustical modeling and Bayesian inference for rigid porous media in the low-mid frequency regime. *The Journal of the Acoustical Society of America*, 144(6):3084–3101, 2018.
- [60] R. Roncen, Z. E. A. Fellah, and E. Ogam. Bayesian inference of human bone sample properties using ultrasonic reflected signals. *The Journal of the Acoustical Society of America*, 148(6):3797–3808, 2020.
- [61] R. Roncen, Z. E. A. Fellah, E. Piot, F. Simon, E. Ogam, M. Fellah, and C. Depollier. Inverse identification of a higher order viscous parameter of rigid porous media in the high frequency domain. *The Journal of the Acoustical Society of America*, 145(3):1629–1639, 2019.
- [62] APS Selvadurai. The analytical method in geomechanics. *Appl. Mech. Rev.*, 60(3):87–106, May 2007.
- [63] D.M. Sullivan. A frequency-dependent FDTD method for biological applications. *IEEE Transactions on Microwave Theory and Techniques*, 40(3):532–539, 1992.
- [64] Daniel Sutliff, David Elliott, Michael Jones, and Thomas Hartley. Attenuation of FJ44 Turbofan Engine Noise with a Foam-Metal Liner Installed Over-the-Rotor. In *15th AIAA/CEAS Aeroacoustics Conference (30th AIAA Aeroacoustics Conference)*. American Institute of Aeronautics and Astronautics, may 2009.
- [65] T. Toulorge and W. Desmet. Optimal Runge–Kutta schemes for discontinuous Galerkin space discretizations applied to wave propagation problems. *Journal of Computational Physics*, 231(4):2067–2091, 2012.
- [66] Miklos Vajta. Some remarks on Padé-approximations. In *Proceedings of the 3rd TEMPUS-INTCOM Symposium*, volume 242, 2000.
- [67] D. Keith Wilson. Relaxation-matched modeling of propagation through porous media, including fractal pore structure. *The Journal of the Acoustical Society of America*, 94(2):1136–1145, 1993.
- [68] D.K. Wilson. Simple, relaxational models for the acoustical properties of porous media. *Applied Acoustics*, 50(3):171–188, 1997.
- [69] Jiangming Xie, Miao-Jung Yvonne Ou, and Liwei Xu. A Discontinuous Galerkin Method for Wave Propagation in Orthotropic Poroelastic Media with Memory Terms. *Journal of Computational Physics*, 397:108865, 2019.
- [70] R. Zamponi, S. Satcunanathan, S. Moreau, D. Ragni, M. Meinke, W. Schröder, and C. Schram. On the role of turbulence distortion on leading-edge noise reduction by means of porosity. *Journal of Sound and Vibration*, 485:115561, 2020.
- [71] Jing Zhao, Ming Bao, Xiaolin Wang, Hyojin Lee, and Shinichi Sakamoto. An equivalent fluid model based finite-difference time-domain algorithm for sound propagation in porous material with rigid frame. *The Journal of the Acoustical Society of America*, 143(1):130–138, 2018.
- [72] Jing Zhao, Zhifei Chen, Ming Bao, and Shinichi Sakamoto. Prediction of sound absorption coefficients of acoustic wedges using finite-difference time-domain analysis. *Applied Acoustics*, 155:428–441, 2019.
- [73] Cornelis Zwikker and Cornelis Willem Kosten. *Sound absorbing materials*. Elsevier publishing company, 1949.